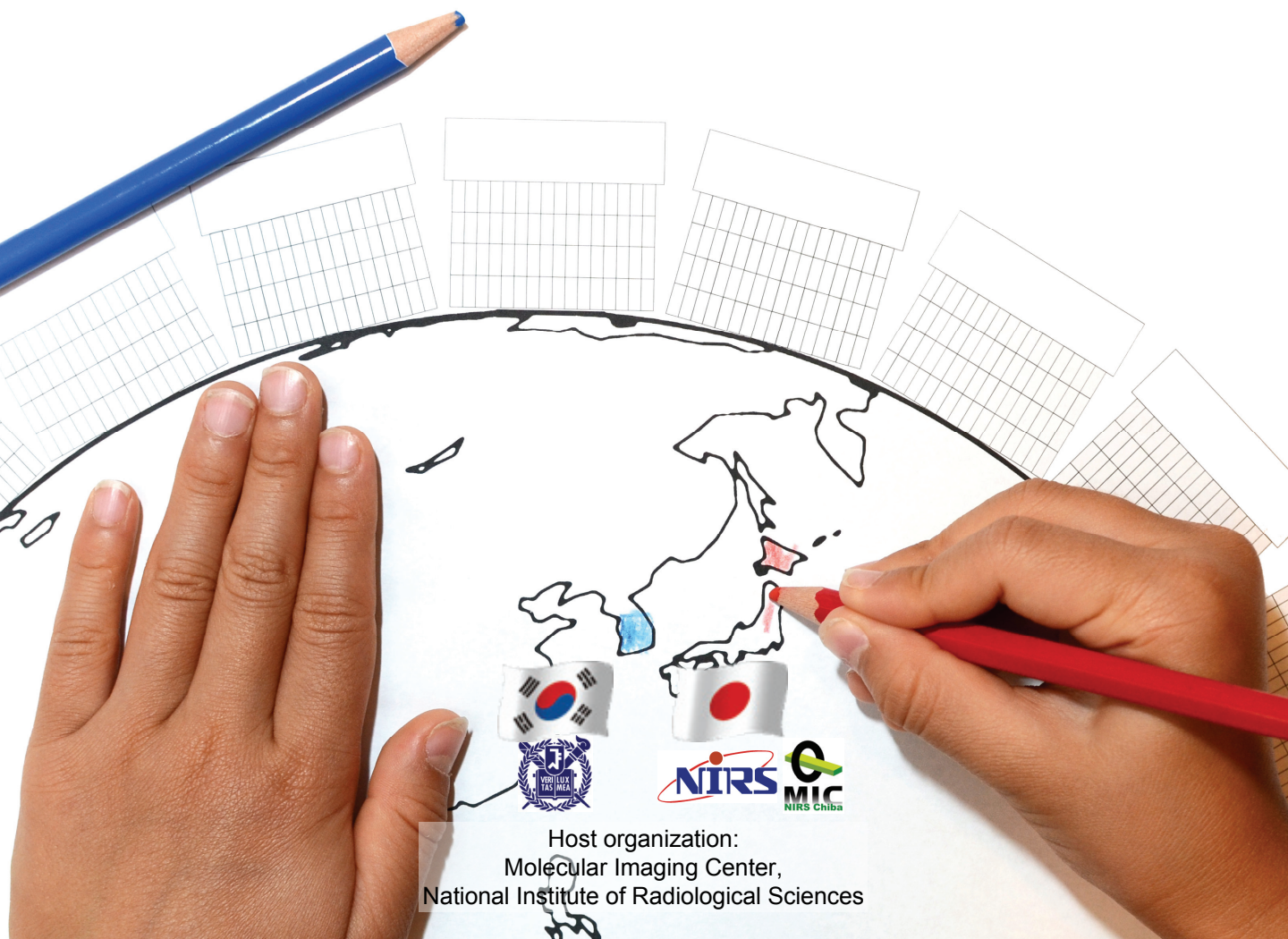# Proceedings of the
# 1st NIRS-SNU Workshop
## on
## Nuclear Medicine Imaging Science and Technology

**26 January 2012**
National Institute of Radiological Sciences, Chiba, Japan



Host organization:
Molecular Imaging Center,
National Institute of Radiological Sciences

# Welcome

We are very pleased to organize the 1st National Institute of Radiological Sciences (NIRS) - Seoul National University (SNU) Workshop on Nuclear Medicine Imaging Science and Technology. The purpose of the workshop is to promote a closer relationship between Korea and Japan, and by sharing our accumulated scientific knowledge, we hope to develop a major hub for state-of-the-art research in the field of nuclear medicine imaging science and technology for Asia and eventually the world. Research topics in this workshop include detectors, image reconstruction methods and systems for nuclear medicine, and new applications such as PET/MRI, Compton imaging and radiotherapy imaging. The workshop will be held annually, with the first workshop to be held at NIRS, Japan, and the second workshop to be held in Korea next year.

**Jae Sung Lee, Ph.D.**
Associate Professor,
Department of Nuclear Medicine,
Seoul National University College of Medicine
jaes@snu.ac.kr

**Taiga Yamaya, Ph.D.**
Team Leader,
Biophysics Program, Molecular Imaging Center,
National Institute of Radiological Sciences
taiga@nirs.go.jp

## 1st NIRS-SNU Workshop on Nuclear Medicine Imaging Science and Technology

**January 26, 2012 (Thursday)**

| | |
|---|---|
| Venue | Lecture Hall, Research Building for Charged Particle Therapy, National Institute of Radiological Sciences (NIRS), Chiba, Japan (http://www.nirs.go.jp/ENG/outline/map/maps_01.shtml) |
| Chair organizers | Jae Sung Lee, Ph.D., Associate Professor, Seoul National University (SNU) College of Medicine |
| | Taiga Yamaya, Ph.D., Team Leader, National Institute of Radiological Sciences (NIRS) |
| Host organization | Molecular Imaging Center (MIC), National Institute of Radiological Sciences |
| Registration fee | Free (Joint Reception will be charged) |
| Language | English |

### Opening

| 13:00 | Openning address | Yoshiharu Yonekura | President, NIRS |
|---|---|---|---|

### Key lecutures — Moderator: T. Yamaya (NIRS)

| 13:05 | Research leading to next generation PET scanners | Taiga Yamaya | NIRS |
|---|---|---|---|
| 13:35 | Overview of nuclear medicine physics and engineering research in Seoul National University | Jae Sung Lee | SNU |
| 14:05 | Break (5 min) | | |

### Special lectures — Moderator: H. Murayama (NIRS)

| 14:10 | Si-PM-PET/MRI: problems and solutions | Seiichi Yamamoto | Kobe City College of Technology, Japan |
|---|---|---|---|
| 14:50 | Simultaneous PET-MR imaging using a short optical fiber bundle | Seong Jong Hong | Eulji University, Korea |
| 15:30 | Development of Compton camera and its application studies for biology and medicine | Naoki Kawachi | Japan Atomic Energy Agency, Japan |
| 16:10 | Break (20 min) | | |

### Presentations — Moderators: J. S. Lee (SNU) and T. Yamaya (NIRS)

| 16:30 | Development of SiPM block detector for TOF PET | Sun Il Kwon | SNU |
|---|---|---|---|
| 16:45 | The X'tal cube PET detector using a monolithic scintillator segmented by laser processing | Naoko Inadama | NIRS |
| 17:00 | Analog signal multiplexing methods for SiPM based position sensitive PET block detectors | Hyun Suk Yoon | SNU |
| 17:15 | Development of DOI-PET detector integrated with RF coil for PET-MRI | Fumihiko Nishikido | NIRS |
| 17:30 | Development of SiPM PET combined with 9.4 T animal-dedicated MRI | Guen Bae Ko | SNU |
| 17:45 | Development of the small OpenPET prototype and its real-time imaging system | Hideaki Tashima | NIRS |
| 18:00 | Accelerated shift-variant resolution recovery reconstruction for Compton camera | Soo Mee Kim | SNU |

### Closing

| 18:15 | Closing remarks | Hiroshi Ito | Biophysics Program Director, NIRS |
|---|---|---|---|

Joint Reception 18:20-19:30 (B1F floor in the Research Building for Charged Particle Therapy)

# Contents

# Research leading to next generation PET scanners

Taiga Yamaya

Molecular Imaging Center, National Institute of Radiological Sciences, Japan

## Abstract

In this paper, main research topics of Imaging Physics Team in NIRS, such as depth-of-interaction detectors, the X'tal cube detector and the OpenPET, are briefly introduced.

## 1. Introduction

Positron emission tomography (PET) is a promising method to promote molecular imaging research as well as cancer diagnosis. However there are still strong demands for higher resolution, higher sensitivity and lower cost. In Imaging Physics Team, therefore, we are carrying out basic studies on instrumentation, image reconstruction and data corrections to improve image quality and quantity in nuclear medicine. In particular, depth-of-interaction (DOI) measurement is essential to achieve both higher resolution and higher sensitivity (Figure 1). We have established our original, novel DOI encoring method based on the reflector control [1][2][3], and we have shown its potential by developing a brain prototype scanner, jPET-D4 [4]. At present, based on our core technologies for DOI measurement, we are developing a next generation DOI detector X'tal Cube and [5] a new equipment concept OpenPET [6].
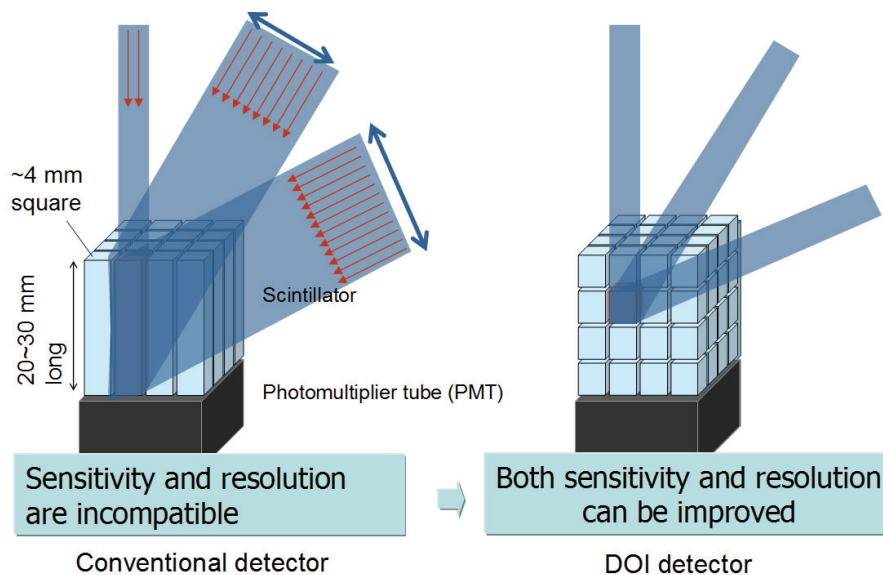


Figure 1. Comparison between a conventional PET detector and the depth-of-interaction (DOI) detector.

## 2. X'tal cube detector

The recent development of small semiconductor photo-detectors such as Geiger-mode avalanche photodiodes (or silicon photomultipliers (SiPMs)), that can replace conventional photomultiplier tubes (PMTs), is leading researchers to make available new PET detectors. For example, insensitivity to magnetic fields enables their use in the development of PET-MRI[7][8][9]. On the other hand, we are developing a next generation PET detector X 'tal cube, which is aimed at making full use of SiPM's potential. The challenging aspect of this work is implementing effective detection of scintillation photons by optically covering all 6 surfaces of a segmented crystal block with multi-pixel photon counters (MPPCs) (Figure 2). At this development stage, we have succeeded to realize an ultimate detector with 1.0 mm$^3$ cubic crystal[5] (Figure 3). The crystal block was composed of a $16 \times 16 \times 16$ array of lutetium gadolinium oxyorthosilicate (LGSO) crystals $0.993 \times 0.993 \times 0.993$ mm$^3$ in size. The crystals were optically glued together without inserting any reflector inside and 96 MPPCs (Hamamatsu S10931-50P, i.e. six faces each with a $4 \times 4$ array of MPPCs), each having a sensitive area of $3.0 \times 3.0$ mm$^2$, were optically coupled to the surfaces of the crystal block. Almost all 4096 crystals were identified through the Anger-type calculation. As a modification toward practical use in terms of assembling efficiency and production costs, we are trying to apply a sub-surface laser engraving technique[10], which can be used to fabricate 3D grids into a monolithic crystal block. We have observed that the laser-processed crystal block has a potential for getting an appropriate diffusion characteristic of scintillation photons[11].
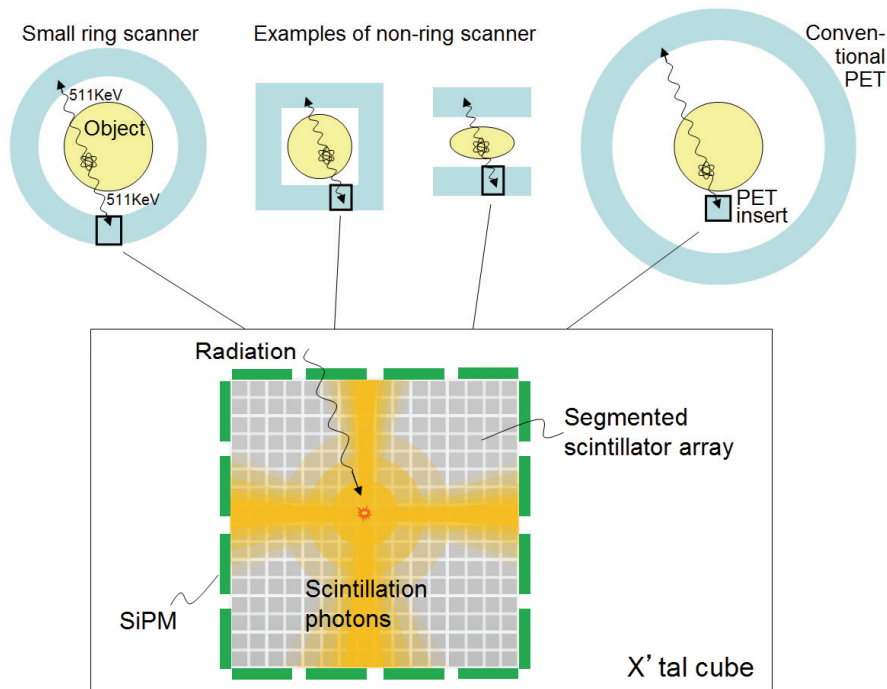


Figure 2. A conceptual sketch of the X'tal cube detector. The challenging aspect of this detector is implementing effective detection of scintillation photons by covering six faces of a segmented crystal block with SiPMs. The isotropic-3D positioning performance is expected to enable various new detector arrangements as well as conventional ring-type arrangements.
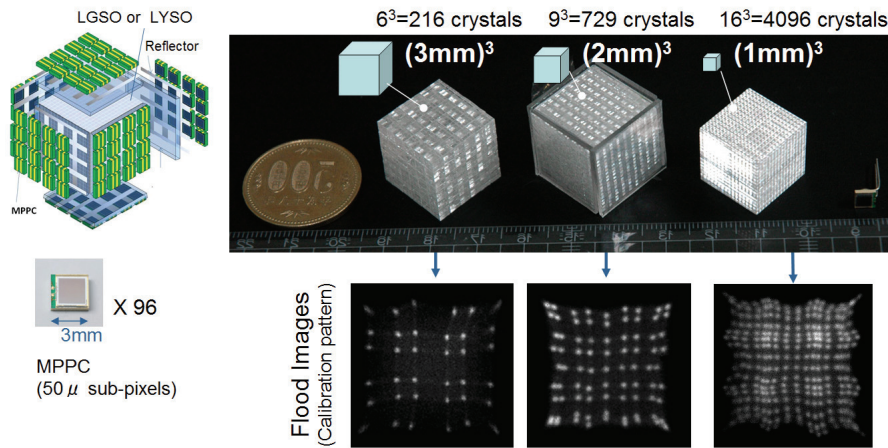
Figure 3. Experimental results of three prototype X'tal cube detectors, based on $(3\ mm)^3$ cubic crystals, $(2\ mm)^3$ cubic crystals and $(1\ mm)^3$ cubic crystals. 2D images corresponding to the middle plane of the crystal arrangement, extracted from the 3D flood histogram images are shown.

## 3. OpenPET

An open-type geometry for PET, OpenPET, is our new idea to visualize a physically opened space between two detector rings[6] (Figure 4). Axial spatial resolution, which is degraded with the extended gap due to the parallax error, can be recovered by use of DOI detectors. The OpenPET is expected to enable joint PET imaging and radiation therapy by letting the beams pass though the gap. For charged particle therapy, in particular, the OpenPET will enable *in situ* dose verification by visualizing the distribution of primary particles stopped in a patient body. PET-based image guided radiation therapy including mobile tumor tracking will become possible by applying a real-time image reconstruction system to be developed [12]. The OpenPET is also expected to enable extension of an axial field-of-view (FOV) with a limited number of detectors [13].
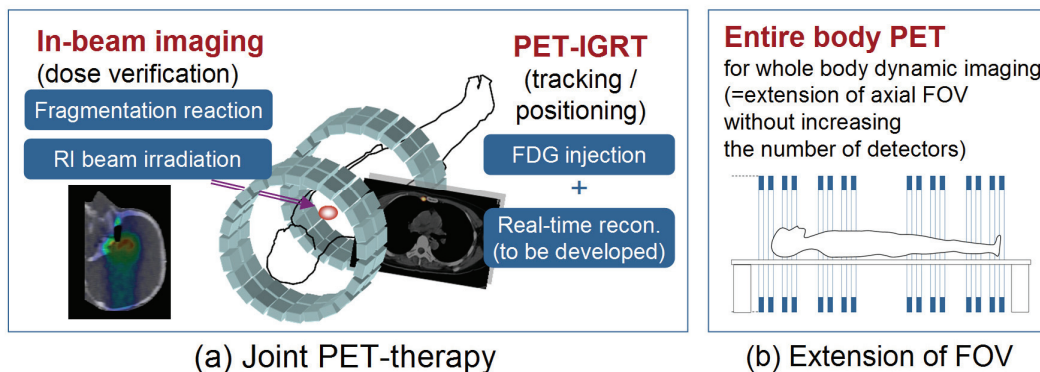


Figure 4. The OpenPET geometry and its applications for joint PET imaging and radiotherapy (a) and extension of the axial field-of-view (FOV) (b).

At this stage, we have developed the first small prototype to show a proof-of-concept of OpenPET imaging [14]. Two detector rings of 110 mm diameter and 42 mm axial length were placed with a gap of 42

mm. For a proof-of-concept of *in situ* dose verification, we carried out the in-beam tests in the heavy ion medical accelerator in Chiba (HIMAC) to visualize the distribution of primary particles stopped in a phantom. For usual carbon ($^{12}$C) beam irradiation, it has been reported that the activity of positron emitters produced through fragmentation reactions is generally low, in addition to the theoretical difference between the dose distribution and positron emitters distribution [15]. Instead of the $^{12}$C beam, therefore, we used a $^{11}$C radioactive beam as an incident beam directly in the secondary beam port, where various radioactive beams can be generated as secondary beams from the $^{12}$C beam by irradiating a $^{7}$Be target [16]. We succeeded to show PET images corresponding to dose distribution (Figure 5).
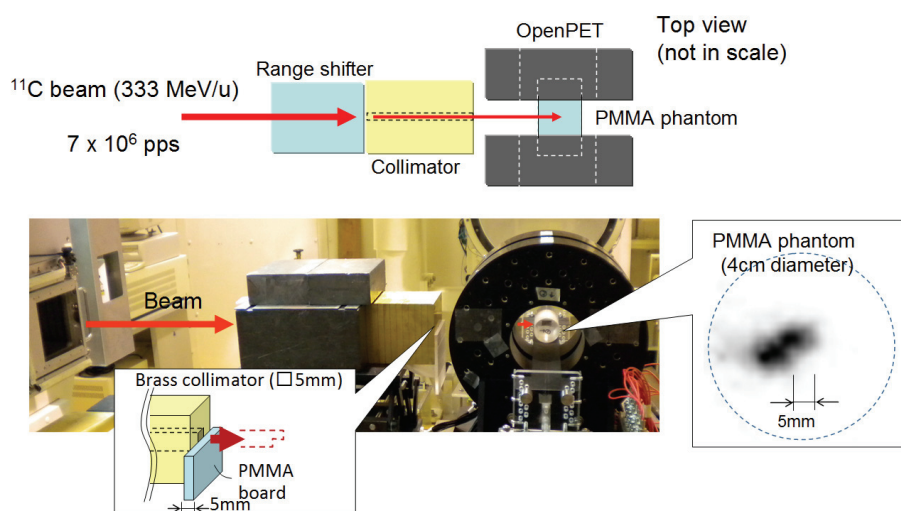


Figure 5. In-beam imaging tests of the developed small OpenPET prototype in the heavy ion medical accelerator in Chiba (HIMAC). 5 mm deference in the range, which was given by adding 5 mm thick PMMA board that covers half the collimated beam, is successfully visualized in the reconstructed image.

## 4. Conclusions

DOI measurement is an essential technology for PET to achieve higher spatial resolution with maintaining higher sensitivity. As a next generation DOI detector, we are developing the X'tal cube, which is a novel, SiPM-based isotropic-3D PET detector. The DOI measurement is also enabling flexible detector arrangement such as the OpenPET.

## Acknowledgements

# References

[1]    H. Murayama, H. Ishibashi, H. Uchida, et al., "Depth encoding multicrystal detectors for PET," IEEE Trans. Nucl. Sci., 45, pp. 1152-1157, 1998.

[2]    N. Inadama, H. Murayama, T. Omura, et al., "A depth of interaction detector for PET with GSO crystals doped with different amounts of Ce," IEEE Trans. Nucl. Sci., 49, pp. 629-633, 2002.

[3]    T. Tsuda, H. Murayama, K. Kitamura, et al., "A four-layer depth of interaction detector block for small animal PET," IEEE Trans. Nucl. Sci., 51, pp. 2537-2542, 2004.

[4]    T. Yamaya, E. Yoshida, T. Obi, et al., "First human brain imaging by the jPET-D4 prototype with a pre-computed system matrix," IEEE Trans. Nucl. Sci., 55, pp. 2482-2492, 2008.

[5]    T. Yamaya, T. Mitsuhashi, T. Matsumoto, et al., "A SiPM-based isotropic-3D PET detector X'tal cube with a three-dimensional array of 1 mm$^3$ crystals," Phys. Med. Biol., 56, pp.6793-6807, 2011.

[6]    T. Yamaya, T. Inaniwa, S. Minohara, et al., "A proposal of an open PET geometry," Phys. Med. Biol. 53, 757-773, 2008.

[7]    S. J. Hong, I. C. Song, M. Ito, et al., "An investigation into the use of Geiger-mode solid-state photomultipliers for simultaneous PET and MRI application," IEEE Trans. Nucl. Sci. 55, pp. 882-888, 2008.

[8]    J. Kang, Y. Choi, K. J. Hong et al., "A feasibility study of photosensor charge signal transmission to preamplifier using long cable for development of hybrid PET-MRI," Med. Phys., 37, pp. 5655-5664, 2010.

[9]    S. Yamamoto, H. Watabe, Y. Kanai, et al., "Interference between PET and MRI sub-systems in a silicon-photomultiplier-based PET/MRI system," Phys. Med. Biol., 56, pp. 4147-4159, 2011.

[10]   T. Moriya, K. Fukumitsu, T. Sakai, et al., "Development of PET detectors usingmonolithic scintillation crystals processed with sub-surface laser engraving technique," IEEE Trans. Nucl. Sci. 57, 2455–2459, 2010.

[11]   N. Inadama, H. Murayama, F. Nishikido, et al., "Performance evaluation of the X'tal cube PET detector using a monolithic scintillator segmented by laser processing," J. Nucl. Med. 52 (Suppl. 1) 322, 2011.

[12]   H. Tashima, E. Yoshida, S. Kinouchi, et al., "Real-time Imaging System for the OpenPET," IEEE Trans.Nucl. Sci., to be published, 2012.

[13]   T. Yamaya, E. Yoshida, N. Inadama, et al, "A multiplex "OpenPET" geometry to extend axial FOV without increasing the number of detectors," IEEE Trans. Nucl. Sci., 56, pp. 2644-2650, 2009.

[14]   T. Yamaya, E. Yoshida, T. Inaniwa, et al., "Development of a small prototype for a proof-of-concept of OpenPET imaging," Phys. Med. Biol., 56, pp. 1123-1137, 2011.

[15]   P. Crespo, T. Barthel, H. Frais-K¨olbl, at el., "Suppression of random coincidences during in-beam PET measurements at ion beam radiotherapy facilities," IEEE Trans. Nucl. Sci., 52, pp. 980-987, 2005.

[16]   E Urakabe et al, "Spot scanning using radioactive 11C beams for heavy-ion radiotherapy," Japan. J. Appl. Phys., 40, 2540-2548, 2001.

# Overview of Nuclear Medicine Physics and Engineering Research in Seoul National University

Jae Sung Lee

Departments of Nuclear Medicine, Biomedical Sciences, and Brain & Cognitive Sciences,
Seoul National University, Korea

## Abstract

In this talk, I will introduce the Department of Nuclear Medicine at Seoul National University (SNU) and briefly summarize the research topics performed in Functional and Molecular Imaging System Lab (physics and engineering group).

## 1. Introduction to SNU NM

Seoul National University (SNU) was founded on August 27, 1946 by merging ten institutions of higher education around the Seoul area (the first national university in South Korea). SNU, as the continuing leader of higher education in Korea, is committed to becoming a global institution. The University's scientific and academic competence has been internationally recognized. The Times Higher Education ranked Seoul National University 47th in 2009, up from 50th in 2008. SNU has also made numerous contributions to scientific research, especially in IT, BT, and NT technologies. As of 2007, it ranks 24th in the Science Citation Index, the worldwide standard for assessing research capacity.

The Department of Nuclear Medicine (NM) in SNU (http://nm.snu.ac.kr/emain) performs cutting-edge research and comprehensive education through collaborating and networking with outstanding researchers and international parties. Fifteen faculties and over 40 researchers with backgrounds in medicine, physics, chemistry, pharmacology, and biology get involved in multidisciplinary researches. The clinical research improves patient care by developing, applying and conducting clinical trials for new materials and methods using PET/CT, radiopharmaceuticals, imaging analysis, brain receptor imaging, and radio-targeted therapy. The research topics in basic nuclear medicine include the development of new radiopharmaceuticals, new technologies for the analysis of nuclear imaging, and new equipments, such as PET/MRI and small animal PET. Another important advanced research field is in vivo molecular imaging which detects the expression of specific genes, biomarker, and cell trafficking using optical imaging, nano-particles as well as radioisotope. Our department was designated as IAEA Collaborating Center for Nuclear Medicine and Molecular Imaging for research and training at December 2004.

Recent active research topics in SNU NM include:

- Translational research using multifunctional nano-particles for optical/PET/MRI imaging and drug or gene delivery
- Translational research of targeted imaging & therapy using reporter genes, peptides, aptamers and microRNAs

- In vivo cell trafficking of stem cells or immune cells using bioluminescence, fluorescence, radio-labeling, and MRI technology

- Imaging neurochemistry and neuropsychology

- Developing PET/MRI, animal and clinical PET technologies, and image analysis software

- Developing novel radiopharmaceuticals targeting heart, brain, inflammation and diverse cancers

- Test of biodistribution, pharmacokinetics, and efficacy of new drug (including small molecules and bio-drugs) using in vivo imaging

- Clinical trials using angiogenesis PET for cancer and amyloid-beta PET for Alzheimer's disease
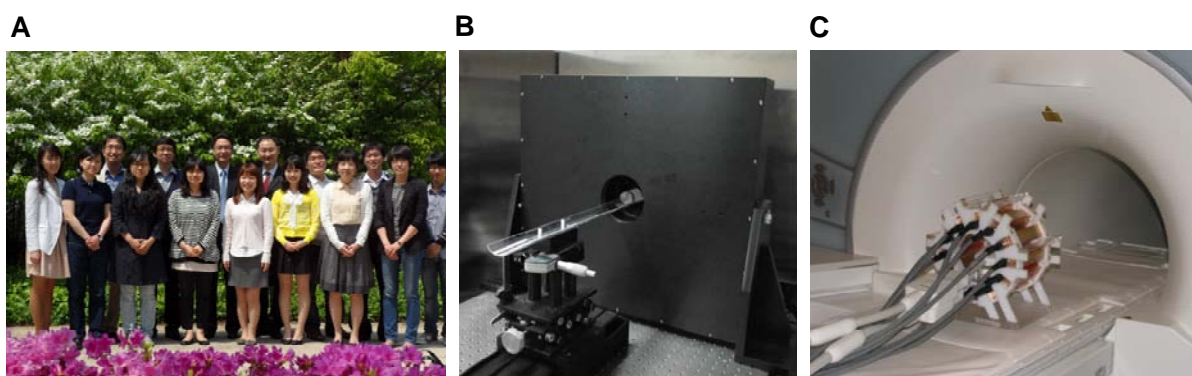


Figure 1. (A) SNU FMISL members. (B) (C) Small animal PET and MR-compatible SIPM PET scanners developed in FMISL

## 2. SNU Functional and Molecular Imaging System Lab (FMISL)

In SNU Department of Nuclear Medicine, the FMISL is the physics and engineering group led by Prof. Jae Sung Lee, PhD. The research goal that FMISL pursue is to develop the technologies with which we can acquire the biologically relevant and clinically useful information from human body and living animals. Our current research interests included, but are not limited to, novel medical imaging systems, i.e. hybrid PET-MRI scanner, and advanced biomedical image analysis technologies. We are especially focusing on the radiotracer imaging modalities, such as positron emission tomography (PET) and single photon emission computed tomography (SPECT).

Major research projects performed at FMISL through the research grants funded by Korean government includes:

- Image processing techniques for Compton camera and application to molecular imaging (Atomic Energy R&D Program of the Korean Science and Engineering Foundation, 6/1/2005~3/31/2011)

- High resolution small animal PET systems with three-layer scintillation crystals (Basic Research Program of Korean Science and Engineering Foundation, 3/1/2006~2/28/2009)

- Basic GMPD PET detector technology for PET/MRI (Atomic Energy R&D Program of the Korean Science and Engineering Foundation, 3/1/2007~2/28/2010)

- Digital positron emission mammography system (Atomic Energy R&D Program of the Korean Science and Engineering Foundation, 7/1/2008~6/30/2013)

- Core technologies for time-of-flight PET (Atomic Energy R&D Program of the Korean Science and Engineering Foundation, 7/1/2010~6/30/2013)
- Image processing algorithms and software for integrated PET/MRI system (Ministry of Knowledge Economy, 10/1/2007~6/30/2012)

## Selected Publications

[1] J. S. Lee. K. W. Kang. PET/MRI. In: E. E. Kim, M. C. Lee, T. Inoue, W-H. Wong, eds. Clinical PET and PET/CT: Principles and Applications. Springer; 2012.

[2] J. S. Lee, S. J. Hong, Geiger-mode avalanche photodiodes for PET/MRI. In: K. Iniewski, eds. Electronic Circuits for Radiation Detection. CRC Press LLC; 2010:179-200

[3] S. Ahn, S. M. Kim, J. Son, D. S. Lee, and J. S. Lee. "Gap compensation during PET image reconstruction by constrained, total variation minimization," Med. Phys., [in press]

[4] H. S. Yoon, G. B. Ko, S. I. Kwon, C. M. Lee, M. Ito, I. C. Song, D. S. Lee, S. J. Hong, and J. S. Lee. "Initial results of simultaneous PET/MRI experiments with an MR-compatible silicon photomultiplier PET scanner," J. Nucl. Med., [in press]

[5] C. M. Lee, S. I. Kwon, G. B. Ko, M. Ito, H. S. Yoon, D. S. Lee, S. J. Hong, and J. S. Lee, "A novel compensation method for the anode gain non-uniformity of multi-anode photomultiplier tubes," Phys. Med. Biol., vol. 57, pp. 191-207, 2011.

[6] S. I. Kwon, J. S. Lee, H. S. Yoon, M. Ito, G. B. Ko, J. Y. Choi, S. H. Lee, I. Chan Song, J. M. Jeong, D. S. Lee, and S. J. Hong, "Development of small-animal PET prototype using silicon photomultiplier (SiPM): initial results of phantom and animal imaging studies," J. Nucl. Med., vol. 52, pp. 572-9, 2011.

[7] S. M. Kim, J. S. Lee, C. S. Lee, C. H. Kim, M. C. Lee, D. S. Lee, and S. J. Lee, "Fully three-dimensional OSEM-based image reconstruction for Compton imaging using optimized ordering schemes," Phys. Med. Biol., vol. 55, pp. 5007-27, 2010.

[8] M. Ito, J. S. Lee, M. J. Park, K. S. Sim, and S. J. Hong, "Design and simulation of a novel method for determining depth-of-interaction in a PET scintillation crystal array using a single-ended readout by a multi-anode PMT," Phys. Med. Biol., vol. 55, pp. 3827-41, 2010.

[9] S. J. Kim, J. S. Lee, K. C. Im, S. Y. Kim, S. A. Park, S. J. Lee, S. J. Oh, D. S. Lee, and D. H. Moon, "Kinetic modeling of 3'-deoxy-3'-18F-fluorothymidine for quantitative cell proliferation imaging in subcutaneous tumor models in mice," J. Nucl. Med., vol. 49, pp. 2057-66, 2008.

[10] S. J. Kim, J. S. Lee, Y. K. Kim, J. Frost, G. Wand, M. E. McCaul, and D. S. Lee, "Multiple linear analysis methods for the quantification of irreversibly binding radiotracers," J. Cereb. Blood. Flow. Metab., vol. 28, pp. 1965-77, 2008.

# Si-PM-PET/MRI: problems and solutions

Seiichi Yamamoto

Kobe City College of Technology, Japan

## Abstract

The silicon-photomultiplier (Si-PM) is a promising photodetector, especially for integrated PET/MRI systems, due to its small size, high gain, and low sensitivity to static magnetic fields. The major problem using a Si-PM-based PET system within the MRI system is the interference between the PET and MRI. We measured these on PET and MRI for better understanding on interference and for developing Si-PM based PET/MRI systems. In addition, the temperature dependent gain, effect of radiofrequency (RF) shield of Si-PM PET will also be discussed.

## 1. Introduction

Recently, development of Si-PM PET systems becomes a emerging field in medical imaging and some groups are now developing their Si-PM based PET systems [1]. We also developed a Si-PM-based depth-of-interaction (DOI) PET system for small animals [2] and successfully conducted the simultaneous measurements with Si-PM PET and MRI system [3]. One possible problem with using the Si-PM-based PET system insert within the MR magnet is the interference between the PET and MRI systems. However, interference between Si-PM-based PET system and MRI system has not yet been systematically evaluated. In this paper, we measured the interference with PET by MRI as well with MRI by PET in a combined Si-PM-based PET/MRI system [4]. The temperature dependent gain [5], effect of radiofrequency (RF) shield of Si-PM PET will also be presented in the talk.

## 2. Methods

### 2.1 Si-PM-based PET system

Figure 1 (A) is a photograph of the Si-PM-based PET system we developed [2]. Si-PM arrays (S11064-025P, Hamamatsu Photonics, Hamamatsu, Japan), were used for the block detectors of the PET system. The Si-PM array has 4 x 4 channels each 3 x 3mm area. Two types of LGSO scintillators - with of 0.75 mol% cerium (Ce) (decay time:~45ns; 1.1x1.2x5mm) and 0.025 mol% Ce (decay time:~31ns; 1.1x1.2mmx6mm), respectively - were optically coupled in the depth-wise direction to form a depth-of-interaction (DOI)-encoding detector, arranged in 11 (transaxial direction) x 9 (axial direction) detector-element configuration, and the proximal scintillators then optically coupled to the Si-PM array. During the simultaneous measurements, the PET detector ring was removed from the detector ring holder (Fig.1(B)) with the signal and bias voltage cables of the PET system and positioned in the MRI system.
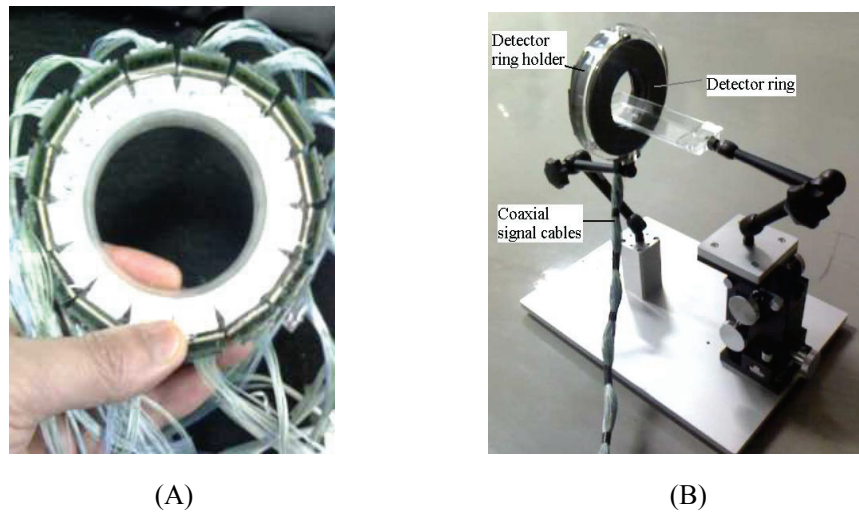
(A)                                    (B)

Figure 1. Detector ring of Si-PM-based PET system without black tape for light shield (A) and Si-PM based PET system with detector ring holder and bed (B).

## 2.2 MRI system

The MRI system used for the simultaneous measurements has a 0.3-T permanent magnet with 170-mm separation (NEOMAX Engineering, Takasaki, Japan). The gradient coils were positioned on the inner sides of the permanent magnets. Between them, a solenoid type RF coil was positioned. We prepared two RF coils, one was with an outer diameter of 42mm and an inner diameter of 40mm (4-cm diameter RF coil), and the other was with an outer diameter of 32mm and an inner diameter of 30mm (3-cm diameter RF coil).

## 2.3 Integrated PET/MRI system

Figure 2 shows a schematic drawing of the integrated Si-PM-based PET/MRI system. The Si-PM-based PET detector ring was positioned at the center of the RF coil of the MRI system. Signals from the Si-PM arrays of the PET detector ring are transferred to the front-end electronics by the small diameter coaxial cables from the side of the MRI magnet. Figures 3 (A) and (B) show photographs of the Si-PM-based PET/MRI system from outside and inside, respectively.
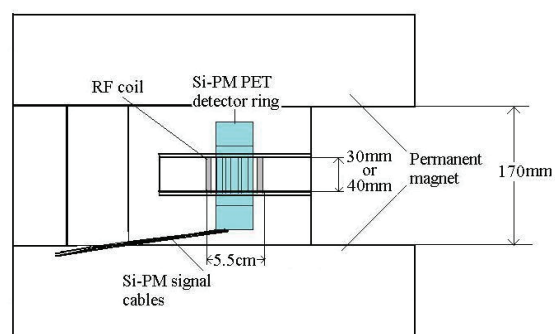


Figure 2. Schematic drawing of integrated Si-PM-based PET/MRI system

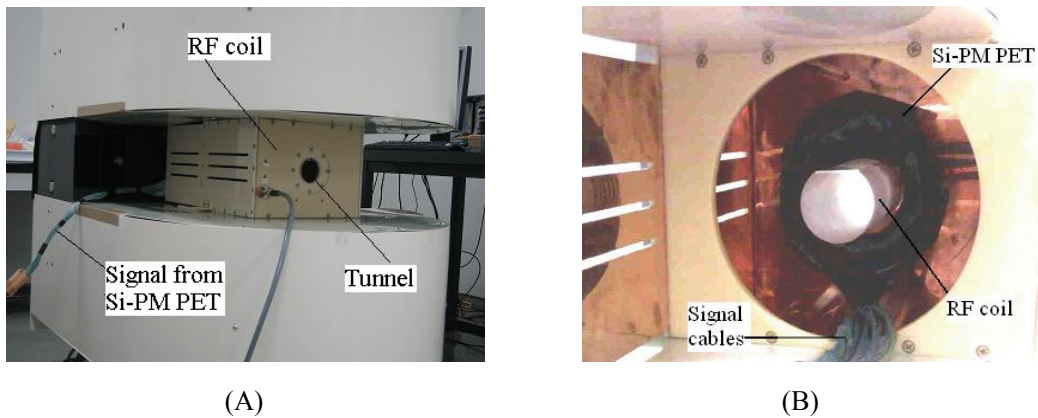(A)                                                    (B)

Figure 3. (A) External view of the Si-PM-based PET/MRI system. (B) Internal view of the system showing the Si-PM PET detector ring positioned around the RF coil of MRI system within the RF shield box.

## 3. Results

### 3.1 Pulse height measurements of RF-induced noise

Figure 4(A) shows the RF-induced pulse observed in the weighted summing signals of the Si-PM-based PET system when the RF power was 43W, and the 4-cm diameter RF coil was used. The maximum amplitude of the noise was ~2000mV, which is higher than the lower energy threshold level (～500mV). Figure 4(B) shows the pulse of the 511-keV gamma photons observed in the weighted summing signals. The RF-induced pulse amplitude was larger than the pulse of the 511-keV gamma photons.



(A)                                                    (B)
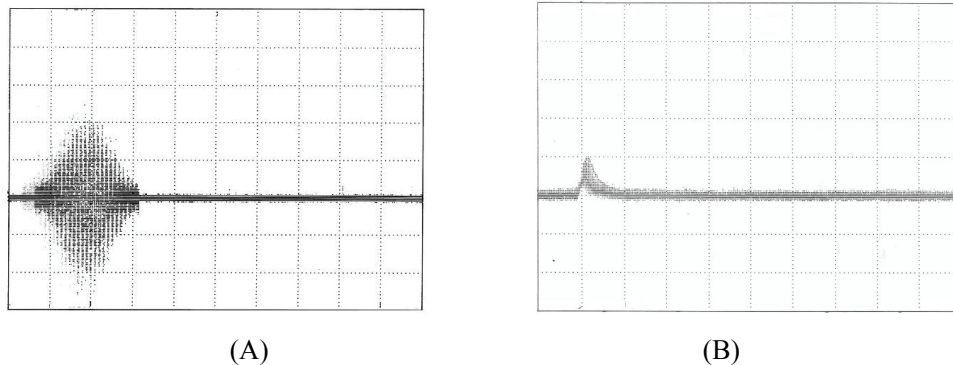
Figure 4. Pulse shape of RF-induced noise observed in weighted summing signals (A). Pulse shape of 511 keV gamma photon pulse (B).

### 3.2 Coincidence count rate measurements of RF-induced noise

Prompt, delayed, and prompt minus delayed count rates of the Si-PM-based PET system as a function of RF power are shown in Fig. 5. When the RF power exceeded the lower energy threshold level (RF power >6W for the 4-cm diameter RF coil, and >50W for the 3-cm diameter RF coil), the prompt, delayed, and prompt minus delayed count rates started to increase.
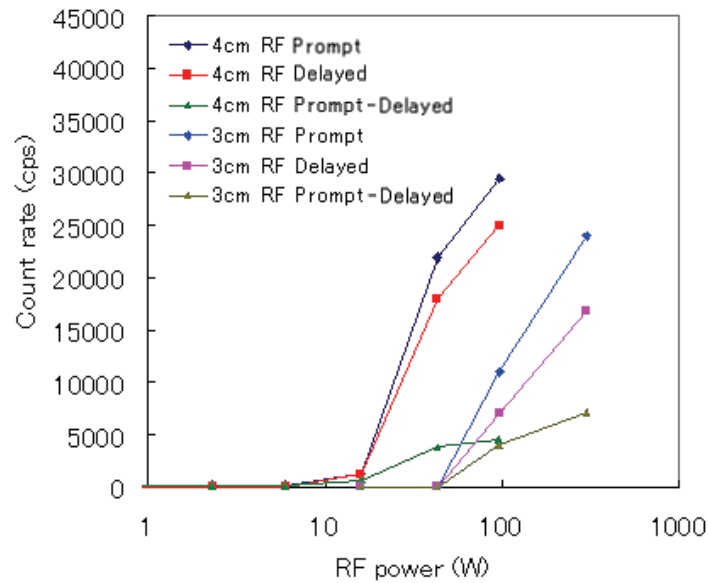
Figure 5. Prompt, delayed, and prompt minus delayed count rates as a function of RF power

## 3.3 Pulse height measurements of RF induced noise as a function of distance from center

The maximum RF induced noise pulse height of the Si-PM-based PET detector ring was measured and evaluated as a function of the distance from the center of the RF coil is shown in Fig.6. The RF-induced pulse height decreased dramatically for both the 3- and 4-cm diameter coils as the distance of the detector ring from the RF coil increased.



Figure 6. Maximum RF- induced pulse height as a function of the distance of the Si-PM detector ring from the center of RF coil

*3.4 Phantom image degradation from noise emission of PET detector ring*

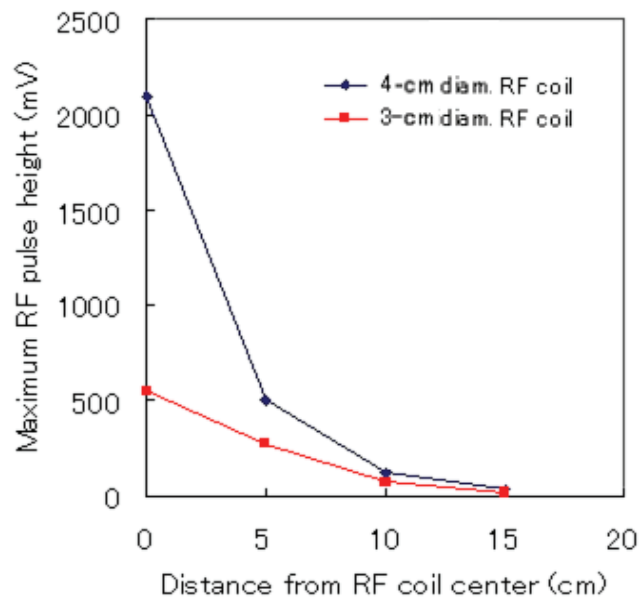MR images of the cylindrical phantom at different distances from the RF coil center are evaluated. The noise was highest when the Si-PM-based PET detector ring was positioned at the center of the RF coil. The noise decreases as the distance from the RF coil center increases. The MR images with 4-cm diameter RF coil were much noisier than those with 3-cm diameter RF coil. The S/Ns with 4-cm diameter RF coil was smaller than that with 3-cm diameter RF coil.

## 4. Discussion

We successfully measured the interference between Si-PM-based PET and MRI systems. The count rates as a function of RF power showed the RF signals could be a serious source of artifacts in the PET reconstructed images. When the RF power exceeded the lower energy threshold level, the count rates started to increase. In practical MRI measurements, the RF power was determined by the transmission tuning, and the power depends on the scan sequences, RF coil diameter, and subject geometry and composition. When the imaging the cylindrical phantom using the FLASH sequence, the RF power was approximately 2.3 to 6W after transmission tuning, which is lower than the lower energy threshold level for both 3- and 4-cm diameter RF coils. Thus, there was no increase in the prompt or delayed count rates caused by the RF-induced noise. However, for scan sequences or conditions requiring higher RF power (e.g. larger objects and larger-diameter RF coils) and producing RF-induced noise of higher amplitude than the threshold level, the noise count rate may be problematic. Another possible method for reducing the interference between PET and MRI is the RF shield around the PET detectors. However, the noise deduction by the RF shield such as copper shield was limited due to the characteristic of the RF signal from the coil. The temperature dependent gain control system is indispensable because some temperature changes dropped the count rate dramatically.

## 5. Conclusions

The interference between integrated Si-PM- PET and MRI systems was significant in terms of the RF-induced noise and artifacts on the PET sinograms and reconstructed images and on the S/N degradation on the MR images. These effects are reduced, however, with increasing distance between the RF coil and the Si-PM-based PET detector ring.

## Acknowledgments

## References

[1]    Kwon SI, Lee JS, Yoon HS, Ito M, Ko GB, et al. Development of small-animal PET prototype using silicon photomultiplier (SiPM): initial results of phantom and animal imaging studies. J Nucl Med. 2011 Apr;52(4):572-9.

[2]    Yamamoto S, Imaizumi M, Watabe T, Watabe H, Kanai Y, Shimosegawa E, Hatazawa J. Development of a Si-PM-based high-resolution PET system for small animals. Phys Med Biol. 2010, 7;55(19):5817-31

[3]    Yamamoto S, Watabe T, Watabe H, Aoki M, Sugiyama E, et al. Simultaneous imaging using Si-PM-based PET and MRI for development of an integrated PET/MRI system. Phys Med Biol. 2011 Dec 14;57(2):N1-N13

[4]    Yamamoto S, Watabe H, Kanai Y, Aoki M, Sugiyama E, Watabe T, et al. Interference between PET and MRI sub-systems in a silicon-photomultiplier-based PET/MRI system. Phys Med Biol. 2011 Jul 7;56(13):4147-59.

[5]    Yamamoto S, Satomi J, Watabe T, Watabe T, Kanai T, Imaizumi M, et al. A temperature-dependent gain control system for improving the stability of Si-PM-based PET systems. Phys Med Biol. 2011 7;56(9):2873-82

# Simultaneous PET-MR imaging using a short optical fiber bundle

Seong Jong Hong[1], Han Gyoo Kang[1], Geun Bae Ko[2], In Chan Song[3] and Jae Sung Lee[2]

[1] Department of Radiological Science, Eulji University, Seongnam, Gyeonggi 461-713, Korea

[2] Department of Nuclear Medicine, College of Medicine, Seoul National University, Seoul 110-744, Korea

[3] Department of Radiology, Seoul National University Hospital, Seoul 110-744, Korea

## Abstract

Optical fibers can serve useful purposes in a PET-MR configuration in which the body coil transmits radiofrequency (RF) waves and the local coil receives RF waves from an imaging object. The optical fibers provide an increased spacing between RF shielded electronic boxes facilitating RF passage to the imaging object and they increase a distance from the imaging object to metallic electronic components. Therefore MR image quality can be improved by using the optical fibers in this PET-MR configuration. We present test results of a SiPM-PET with and without 3-T MR operation.

## 1. Introduction

To achieve simultaneous PET/MR imaging, optical fibers have been used for some time to transfer scintillation lights to photomultiplier tubes, which must be placed at almost zero magnetic field intensity. Latest solid state devices such as avalanche photodiodes and silicon photomultiplier tube are immune from magnetic field and radiofrequency (RF) waves, and it is not necessary to use optical fibers which deteriorate energy and coincident timing resolutions. However, short optical fibers can be used to improve MR image quality in a certain PET-MR configuration without deteriorating energy and coincident timing resolutions too much [1, 2]. We present test results of a SiPM-PET with and without 3-T MR operation, along with MR images obtained with and without the SiPM-PET.

## 2. Methods

### 2.1 SiPM-PET

The SiPM-PET shown in Figure 1 is consisted of 12 SiPM-PET modules, each of which was assembled with a crystal block, an optical fiber bundle, a Hamamatsu MPPC and a signal processing electronics module. The crystal block was assembled with 6x6 LYSO crystals with a dimension of 2.47x2.74x20 mm$^3$, and the optical fiber bundle with ~400 double-clad optical fibers with a length of 31 mm and a diameter of 1.0 mm. Custom jigs were used to assemble the Hamamatsu MPPC, the LYSO crystal block, and the optical fiber bundle into a SiPM-PET detector module. The signal processing electronics module enclosed with a RF shielding box contained 4x8 through holes on one face of the box for 32 MPPC pins. Signals for 12 SiPM-PET modules were sent to the data acquisition system outside the MRI room via nonmagnetic shielded-twist-pair (FTP) cables.
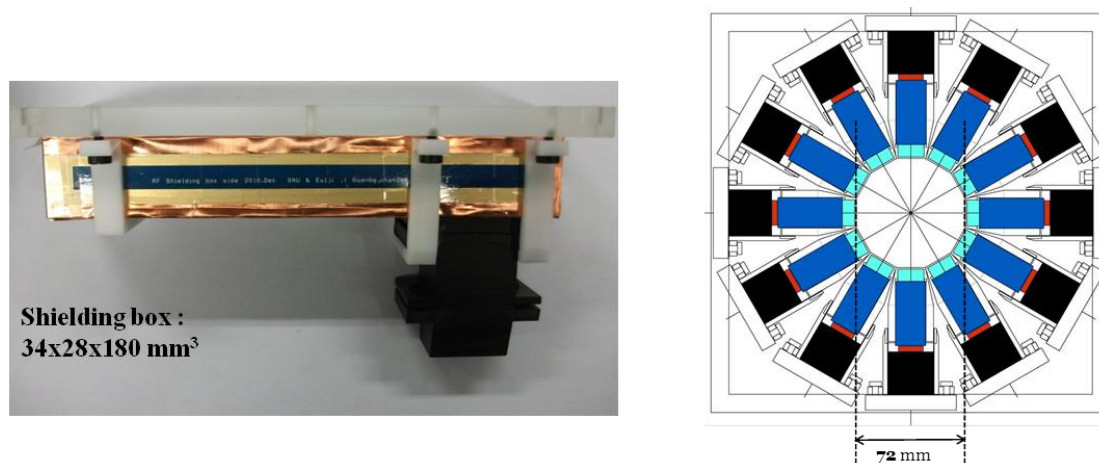
Figure 1. Assembled SiPM-PET module and SiPM-PET layout. The SiPM-PET consists of, from the center to the circumference, the crystal block, the optical fiber bundle, the MPPC and the shielded electronic box.

Two different phantoms were used to evaluate MR image. One phantom was built of gelatin and glass cylinders inside which a MR contrast agent, DOTAREM with a 1:1 mixture with a 0.9% saline solution was put. The other phantom consisted of two syringes filled with water and a cucumber into which a 3.0 mm diameter capillary filled with $^{18}$F solution was inserted.

## 2.2 Experiments and Analysis

We tested the SiPM-PET with MR pulse sequences currently used in clinical diagnosis. The MR pulses sequences were chosen to see T1, T2, and T2* effects on gelatin and water in the two phantoms. During the simultaneous PET-MR imaging, the body coil transmitted the RF pulses to the phantoms while the surface coil received the signals from the phantoms.

All scanned PET data were reconstructed using the maximum likelihood expectation (MLEM) reconstruction. The image fusion of PET and MR was performed using software called FIRE (Functional Image Registration)[3].

## 3.  Results

Crystal map and energy distribution from one of the 12 SiPM-PET modules obtained without 3-T MR operation (3T) and with turbo-spin echo sequence (TSE) and gradient echo sequence (GE) did not show RF interferences due to the MR operation. The MR phantom images of the two syringes and cucumber were similar with and without the 3-T MR operation as shown in Figure 2.

Figure 3 shows a MR phantom (left) and the reconstructed PET image of a capillary tube embedded into a cucumber (right), obtained during simultaneous PET-MR imaging. An overlaid PET-MR image is shown in the center of figure 9.
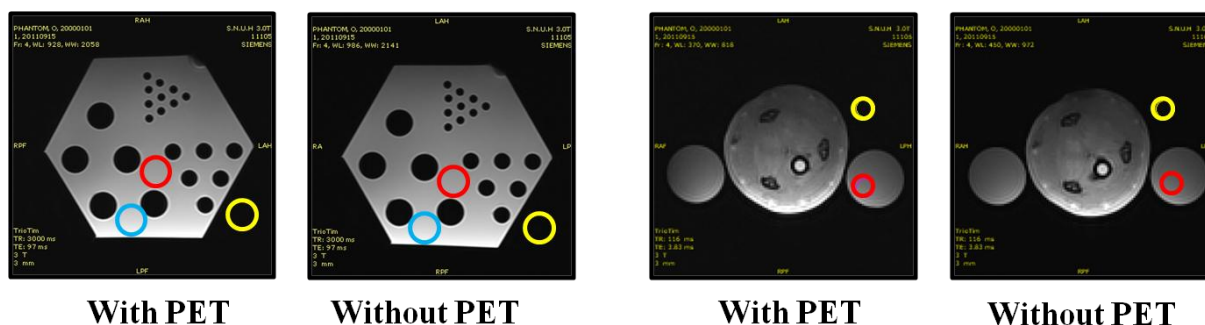
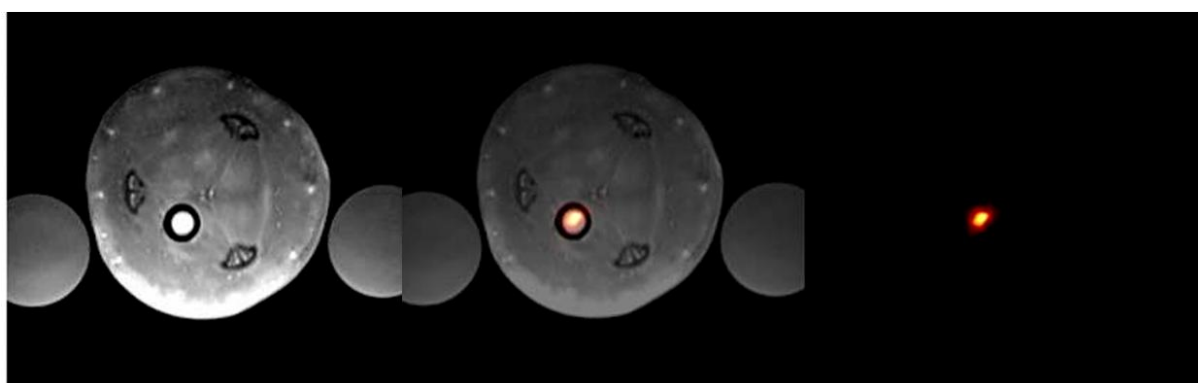Figure 2. Cucumber phantom images with and without the SiPM-PET.



Figure 3. Reconstructed phantom image of the capillary tube imbedded in the cucumber. MR (left), PET (right), and overlaid PET-MR image (center).

## 4. Discussion

A PET-MR system which did not use copper shielding for PET electronics was recently reported[4]. The authors did not observe MR interference and claimed the distance between an imaging object and PET electronics was an important factor. The SiPM-PET system that we developed also increases the distance between the imaging object and electronics by the optical fiber length. This increase might have contributed to the absence of MR interference and it would also help improve the field uniformity near the imaging object, resulting in insignificant differences in MR images with and without the SiPM-PET system.

SiPMs are well known for their strong dependence on temperature and the need to operate at a stable temperature. Enclosing the SiPMs with electronics in the shield box requires cooling for stable operation. Since the SiPM-PET system that we developed places the SiPMs outside the copper shielding box, the SiPMs are at the stable temperature of the MR room and thus they do not need to be actively cooled.

## 5. Conclusions

The proposed SiPM-PET inserted into the 3-T MRI bore did not degrade the MR images during the various MRI sequences, and the MR operation also did not deteriorate the SiPM-PET performance. Using the relatively short optical bundle of 31 mm length, we achieved about 20% energy resolution and 2.0 ns time resolution from the SiPM-PET modules.

In conclusion, the SiPM-PET system which we developed performed well and it can be easily extended for PET/MR imaging of the brain, breast, and other extremities.

## Acknowledgments

## References

[1]    H Kang, G Ko, S Jang, C Kim, H Yoon, M Ito, S Kwon, I Song, J Lee, and S Hong, "A study of simultaneous PET/MR imaging using SiPM PET modules with a short optical fiber bundle," Suppl. to J. Nucl. Med. 52 Suppl. 1, 446, 2011.

[2]    S. Hong, H Kang, G Ko, I Song, J Rhee, and J Lee, "SiPM-PET with a short optical fiber bundle for simultaneous PET-MR imaging," Submitted to Phys. Med. Biol.

[3]    Lee J S, Park K S, Lee D S, Lee C W, Chung J K, Lee M C 2005 Development and applications of a software for functional image registration (FIRE) Comput. Meth. Prog. BioM. 78 157–64

[4]    Vaska P *et al* 2011 An MRI-compatible PET Insert for Whole Body Studies in Rodents at High Functional and Anatomical Resolution in Proc. IEEE Nucl. Sci. Symp. and Med. Imag. Conf., Valencia, Spain, MIC13-1.

# Development of Compton camera and its application studies for biology and medicine.

Naoki Kawachi

Radiotracer Imaging Group, Medical and Biotechnological Application Division,

Quantum Beam Science Directorate, Japan Atomic Energy Agency

## Abstract

The Compton imaging system is a potentially next-generation *in vivo* imaging system and a successor to Positron Emission Tomography (PET) and Single Photon Emission Computerized Tomography (SPECT) systems. In order to achieve Compton imaging, it is necessary to develop technologies that can be used to detect the two major types of an important interaction of γ-ray in matter, *Compton scattering* and *Photoelectric absorption*, and estimate the direction of an incoming γ-ray produced by a radiation source. These techniques are different from the methods used in PET and SPECT with the coincidence of two γ-ray detections and with the physical collimation. Key technologies in our prototype of Compton camera for accurate imaging are usage of Si and CdTe semiconductors, which has been proved to be used observation of high-energy astrophysical phenomena. Some images acquired with the Compton camera will be presented in this talk.

## 1. Introduction

Recent innovations in imaging technology have been making it increasingly easy to examine the structure, function, and state of living organisms. Radionuclide-based imaging elucidates the physiology invisible from the outside of living body by visualizing their elements kinetics, using synthesized radioisotopes (RI) as tracers. It has evolved as an effective method in biology and medicine together with imaging instruments such as positron emission tomography (PET) and single photon emission computed tomography (SPECT). A variety of technological innovations have improved the spatial resolution and sensitivity of these instruments, thus enabling accurate measurement of the tracers' time-course dynamics in three-dimensional space.

Here, we focus on the Compton camera, an imaging system with the additional dimension of "energy". The Compton imaging has a potential of a next-generation imaging system and a successor to PET and SPECT systems. Since this instrument has energy resolution, it can simultaneously acquire images of the dynamic states of multiple compounds, rendering it quite effective. For example, (1) it is expected that the *in vivo* interaction and reaction processes such as the migration and metabolism of multiple elements and molecules can be observed, (2) and that multiple bioactive molecules can be imaged simultaneously by labeling them with different RIs. On the other hand, plant research to solve the environmental and food problems, wide range RI imaging will open up a new field of multi-mineral simultaneous imaging, that were difficult to acquire with conventional method of the bio-imaging analyzer and the positron emitting

tracer imaging system (PETIS)[1,2]. Furthermore, it is possible to significantly increase the types of RIs whose images can be acquired by increasing the energy range, and further innovation in tracer synthesis may lead to further revolution in this field.

## 2. Compton Camera

### 2.1 History

The original concept of the Compton imaging was invented in the early 1970s in astronomical research[3], and it was soon proposed for applying to biological and medical studies[4]. Since then, various types of Compton cameras with various radiation measurement instrumentations have been investigated.

Japanese research groups lead the world in developing the Compton camera as a molecular imaging instrument, and have succeeded in acquiring tracer distribution images *in vivo* and in developing an image-reconstruction method. The GREI is a germanium semiconductor Compton camera developed in RIKEN, which has high energy resolution to detect accurate determination of the scatter angle for γ-ray[5]. A research group of Kyoto Univ. has been developing a Compton camera, which has a new type of the gas detector. The gas detector measures both the recoil γ-ray and the scattered electron, so that higher quality image is provided with less radiation dose[6].
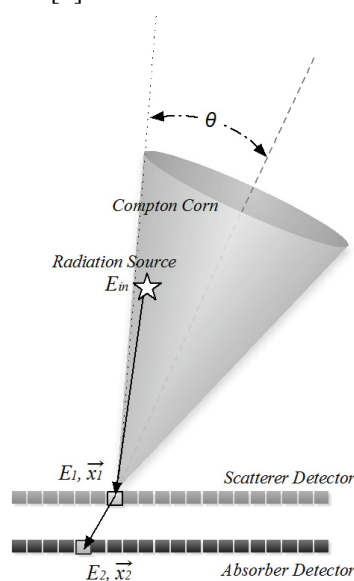


Figure 1. Schematic diagram of the principle of Compton imaging to detect a direction of incoming γ-ray from a radiation source.

Research groups of Japan Atomic Energy Agency (JAEA), Japan Aerospace Exploration Agency (JAXA), and Gunma Univ. are collaborated and undertook the development of a Compton camera aimed at visualizing multiple RI tracers in near field of the camera, using semiconductor detectors with a proven track record in observing cosmic rays[7]. For the establishment of this "medical and biological applied research using Compton cameras" as a new imaging research, a number of issues need to be addressed, such as the development of analytical methods and experimental techniques[8, 9, 10]. In that sense, the present study may be considered just the beginning of research and development.

## 2.2 Principle of Compton Imaging

Compton cameras conduct two-stage γ-ray measurement consisting of Compton scattering and photoelectric absorption, deriving parameters of the source of incident γ-ray from analyzing the kinematics of each interaction. In the first stage, the position ($x_1$) of Compton scattering occurrence in the detector and the energy ($E_1$) imparted to the detector are measured, and in the second stage, the position ($x_2$) of photoelectric absorption of photons after the Compton scattering and the energy ($E_2$) stopped to the detector are measured. Using this primary measurement, the locations of photon sources can be described by a probability distribution called a Compton cone in the field of view (apex: $x_1$, rotational symmetric axis: $x_2$-$x_1$, apex angle: $\theta$), as depicted in Figure 1. The apex angle θ is determined by the imparted energy $E_1$ and the total energy of incident photons ($E_1 + E_2$); the relational equation is represented as follows:

$$\cos\theta = 1 - m_e c^2 \left( \frac{1}{E_2} - \frac{1}{E_1 + E_2} \right)$$

(Equation 1)

In other words, the location of the radiation source to be detected can be calculated from simultaneously measured locations of two interactions in the detector and the energy value. In order to develop the Compton camera, a detector element is required with both high spatial and energy resolutions.

## 3. Si/CdTe Compton camera and its application studies for biology and medicine

A new Compton cameras based on advanced technologies of silicon (Si) and cadmium telluride (CdTe) semiconductor detectors with high spatial and energy resolutions have been developed [11] (Figure 2). Adoptions of such devices are great advantage to the spatial resolution since it depends mainly on precision of the energy and position measurements. Si is good scatterer detector since it yields a large Compton-scattering probability and has a small Doppler broadening effect. On the other hand, CdTe is used as absorber owing to its large cross section of photoelectric absorption.
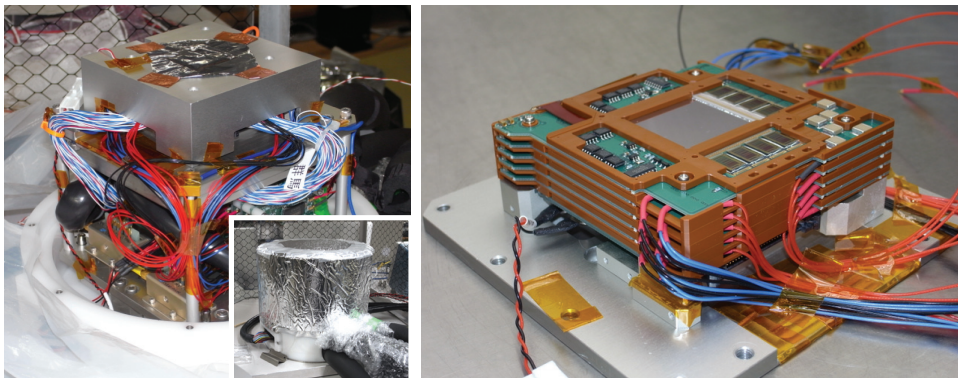


Figure 2. The detector head module of the newly developed Si/CdTe Compton Camera, which is consist of one layered Si dual side strip structured detector (32 mm$^2$, 400 μm thickness, 250 μm pitch) and four layered CdTe dual side strip structured (32 mm$^2$, 500 μm thickness, 250 μm pitch). Each gaps of the detectors is 4 mm.

Using the Si/CdTe Compton camera system, we performed imaging experiments by placing a point gamma source of [133]Ba (364 keV) in a reticular pattern at intervals of 20 mm within an FOV of 300 mm$^3$ in front of the camera. As a result, an intensity distribution map of each source and distorted images point source showing the forms of elliptical object around the corner of the FOV were obtained. Such a distortion and an interval dependencies of spatial resolutions (Figure 3.) are a marked characteristic of Compton imaging at near-field area of camera head for medicine and biology. We will implement a normalization protocol into the LE-EM reconstruction by using measured point-response-functions in each gamma-ray energies.
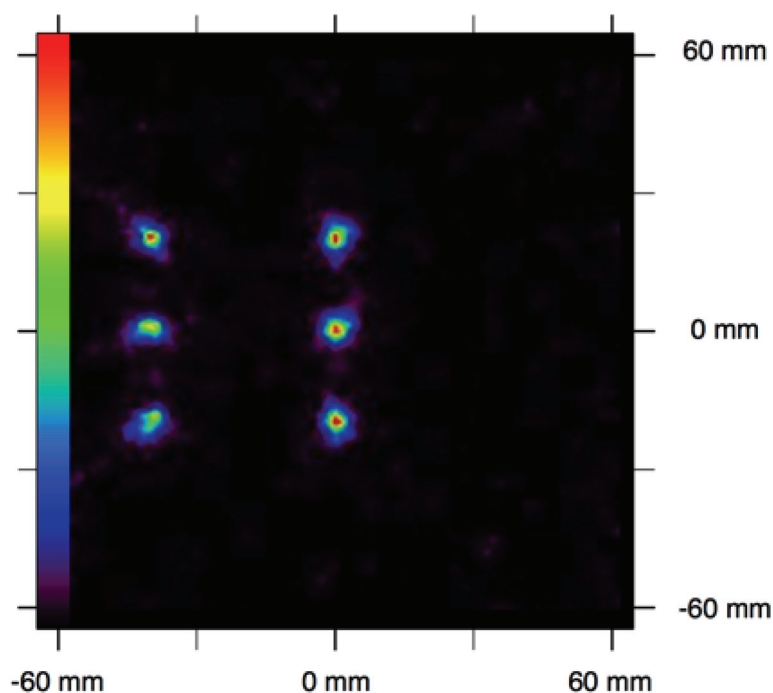


Figure 3. An experimental imaging result by using the novel Si/CdTe Compton Camera with six gamma point sources of [133]Ba (356 keV, 800 kBq), which was placed on the plane of 50 mm distance from the Si detector surface at (-20 mm, 20 mm), (-20 mm, 0 mm), (-20 mm, -20 mm), (0 mm, 20 mm), (0 mm, 0 mm), and (0 mm, -20 mm),). The imaged point sources placed remote from the center of FOV are ellipsoidally-deformed.

## Acknowledgments

## References

[1]  S. Fujimaki, et al., "Tracing cadmium from culture to spikelet: non-invasive imaging and quantitative characterization of absorption, transport and accumulation of cadmium in an intact rice plant," Plant Physiology, 152, pp. 1796-1806, 2010.

[2]  N. Kawachi, et al., "Real-time whole-plant imaging of 11C translocation using positron-emitting tracer imaging," Nucl. Instrum. Methods Phys. Res. A 648, pp. 317-320, 2011.

[3]  S. Kabuki, et al., "Development of electron tracking Compton camera using micro pixel gas chamber for medical imaging," Nucl. Instrum. and Methods. A580, pp. l031-1035, 2007.

[4]  S. Motomura, et al., "Multiple molecular simultaneous imaging in a live mouse using semiconductor Compton camera," J. Analytical Atomic Spectrometry, 23, pp. 1089-1092, 2008.

[5]  V. Schonfelder, A. Hirner and K. Schneider, "A Telecsope for Soft Gamma Ray Astronomy," Nuclear Instruments and method, 107, pp.385-394, 1973.

[6]  R. W. Todd, J. M. Nightingale, and D. B. Everett, "A proposed γ camera," *Nature,* vol. 251, pp. 132–134, 1974.

[7]  T. Takahashi, et al., "High resolution CdTe detectors for the next generation multi-Compton gamma-ray telescope," SPIE 4851, pp. 1228-1235, 2003.

[8]  S. Watanabe, et al., "A Si/CdTe Semiconductor Compton Camera," IEEE Trans. Nucl. Sci., 52, pp. 2045-2051, 2005.

[9]  S. Takeda et al., "Experimental results of the Gamma-ray imaging capability with a Si/CdTe semiconductor Compton camera," IEEE Trans. Nucl. Sci., 56, pp. 783-790, 2009.

[10]  N. Kawachi, "Development of a Prototype Compton Camera for In Vivo Imaging Using Si and CdTe Semiconductor Detectors," Med. Imag. Tech., 27, 1-7, 2009.

[11]  Yamaguchi, M. et al., "Development of head module for multi-head Si/CdTe Compton camera for medical applications," Nucl. Instrum. and Methods. A648, pp. 2-7, 2011.

# Development of SiPM block detector for TOF PET

Sun Il Kwon and Jae Sung Lee

Department of Nuclear Medicine, Seoul National University, Korea

## Abstract

Silicon photomultiplier (SiPM) is a promising semiconductor photo-sensor in PET and PET/MRI with time-of-flight (TOF) capability. Proposed block detector consisted of 3 × 3 16-channel MPPCs and 12 x 12 LYSO crystals and provided row and column signals for energy and timing measurement. Multi-channel digital TDC based on FPGA is developed with ~15 ps/bin TDC time resolution.

## 1. Introduction

Silicon photomultiplier (SiPM) is a promising semiconductor photo-sensor in PET and PET/MRI because it is MRI-compatible and has good timing properties comparable to those of a PMT. Therefore, SiPM is regarded as a suitable photo-sensor for MR-compatible time-of-flight (TOF) PET scanners. In addition, the compact size of SiPM enables the one-to-one coupling between scintillation crystal and photo-sensor to yield best timing performances. However, a large number of electronic components and wires are required for manipulating each individual SiPM channel in large size TOF PET block detectors. In this study, we have investigated the design of a high speed SiPM detector module for TOF PET incorporated with.

## 2. Methods

### 2.1 Signal readout scheme

A proposed SiPM block detector consisted of 3 × 3 16-channel MPPCs, 12 × 12 LYSO crystals, which were directly coupled with MPPCs. The front-end electronic circuit, which was connected with MPPCs, was comprised of two-stage amplifier and ultrafast comparator in each row and column of a block detector. Signal lines were carefully wired to prevent degradation of timing performance due to PCB routing.

### 2.2 Energy and timing performance evaluation

To verify the concept of the proposed signal readout scheme, preliminary experiments were performed using NIM/VME modules. One of 16 channels was connected with the front-end electronic board, and a 3 × 3 × 10 mm LYSO polished crystal wrapped with ESR reflector was coupled with the MPPC channel. An R9800 PMT (Hamamatsu) with 4 × 4 × 10 mm LYSO crystal was used as a reference detector. QDC (V955, Caen) and TDC (N775N, Caen) modules were used to obtain energy and timing performances, respectively. The results were compared with those obtained using conventional timing measurement setup using constant fraction discriminator (CFD, Ortec 935).

## 2.3 Multi-channel digital TDC based on FGPA

We are also under the development of multi-channel digital TDC based on FPGA. Output signals of comparators in front-end circuit board are connected into VIRTEX-6 FPGA (Xilinx) evaluation board. Row signals are used to obtain energy of a gamma-ray event, and column signals are used to detect first few photons of the event for timing measurements. To reduce the complexity of circuit in block detector, energy is measured in FPGA using time-over-threshold method instead of ADC or QDC acquisitions.

The multi-channel digital TDC is developed using delay chain method. In the TDC, the fine counter starts when signal occurs and stops when signal disappears. The FPGA stores start and stop counter values for every single event with coarse counter values.

## 3. Results

### 3.1 Timing resolutions

Figure 1(a) represents the timing resolution of MPPC as a function of threshold voltage of comparator in proposed front-end readout circuit. The best timing resolution was 317.4 ps with a 0.05 V threshold voltage. This was compatible to the timing resolution of same MPPC measured using conventional CFD trigger (326.5 ps). Figure 1(b) shows the timing resolution of MPPC as a function of operating voltage.
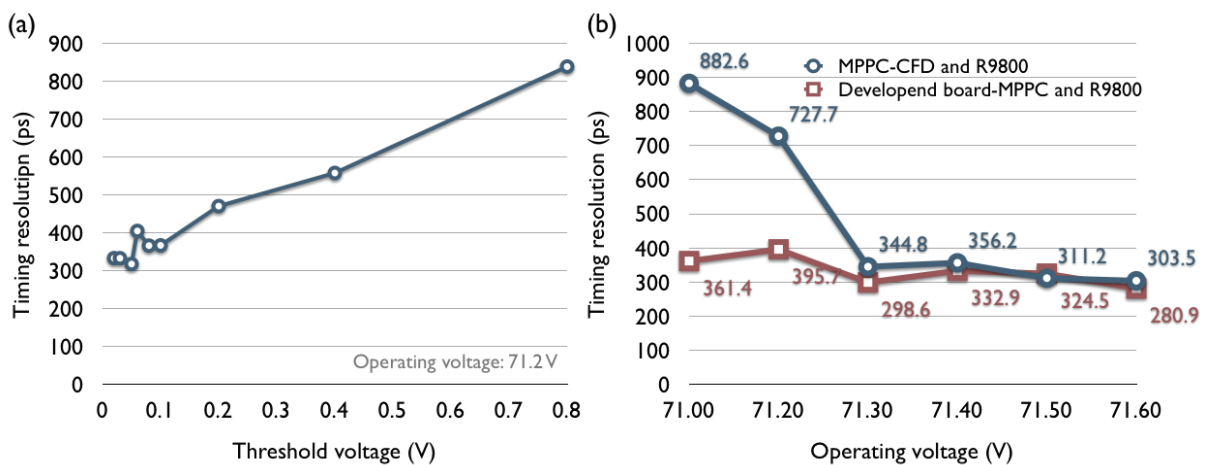


Figure 1. Timing resolution of MPPC as a function of threshold voltage of comparator (a) and operating voltage for MPPC (b). In (b), blue circle represents CFD acquisitions with MPPC signal and red square shows the results using proposed readout scheme.

### 3.2 Energy measurements

Figure 2 shows energy measurement results using QDC and time-over-threshold method. Figure 2(a) represents energy spectrum using QDC module. The results of time-over-threshold method strongly depended on its threshold voltage. Figure 2(b) shows the well-adjusted result, in which the photo-peak and scatter regions are easily resolved. In this condition, time-over-threshold values were proportional to energy measured using QDC (Figure 2(c)).
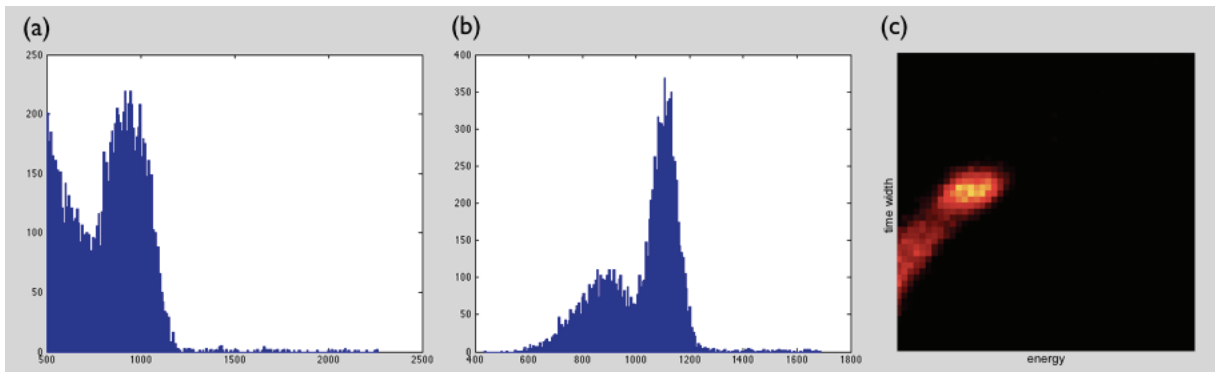
Figure 2. Energy measurement using QDC module (a), time-over-threshold method (b), and relationship between energy and time-over-threshold values (c).

## 3.3 Implementation of multi-channel TDC on FPGA

Figure 3 represents the result of TDC bin value versus delayed time of one channel. Every channel shows linear and stable result with ~15 ps/bin TDC time resolution.
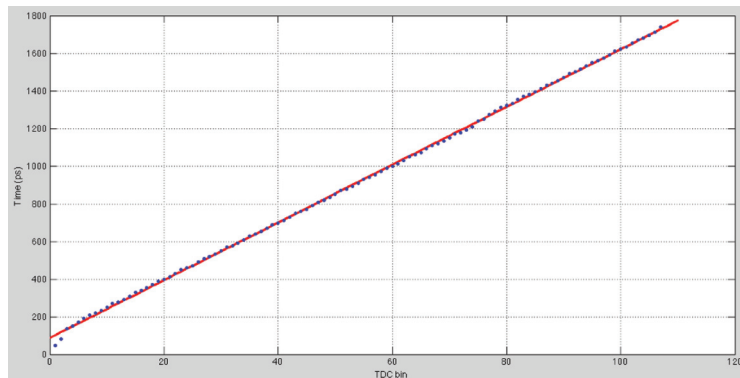


Figure 3. Implemented TDC value versus delayed time. Blue dot indicates real value and red line indicates linear fitting line. Calculated TDC time resolution was 15 ps/bin.

## References

[1] C. L. Kim, G.-C. Wang, and S. Dolinsky, "Multi-Pixel Photon Counters for TOF PET Detector and Its Challenges," *Nuclear Science, IEEE Transactions on,* vol. 56, no. 5, pp. 2580-2585, 2009.

[2] D. R. Schaart, S. Seifert, R. Vinke *et al.*, "LaBr 3 :Ce and SiPMs for time-of-flight PET: achieving 100 ps coincidence resolving time," *Physics in Medicine and Biology,* vol. 55, no. 7, pp. 179-89, 2010.

[3] C. L. Kim, M. D. L., and G. A., "Time-of-Flight PET Detector Based on Multi-Pixel Photon Counter and Its Challenges," *Nuclear Science, IEEE Transactions on,* vol. 58, no. 1, pp. 3-8, 2011.

[4] J. Wu, and Z. Shi, "The 10-ps wave union TDC: Improving FPGA TDC resolution beyond its cell delay." pp. 3440-3446.

[5] V. Chulkov, and A. Medvedev, "An interpolating time-to-digital converter on an FPGA," *Instruments and Experimental Techniques,* vol. 52, no. 6, pp. 788-792, 2009.

# The X'tal cube PET detector
# using a monolithic scintillator segmented by laser processing

Naoko Inadama[1], Takahiro Moriya[2], Hideo Murayama[1],
Fumihiko Nishikido[1], Eiji Yoshida[1], and Taiga Yamaya[1]

[1] Molecular Imaging Center, National Institute of Radiological Sciences, Japan
[2] Hamamatsu Photonics K.K., Japan

## Abstract

The X'tal cube PET detector which we have developed consists of a number of multi-pixel photon counters (MPPCs) and a scintillation crystal block segmented 3-dimensionally into cubes. The MPPCs are coupled to all sides of the crystal block and detects scintillation light originating at a cubic segment by radiation detection. The segment location inside the crystal block is determined by a simple calculation with the MPPC signals. Using a 3-dimensional (3D) array of small cubic crystals for the crystal block, we have already proved sufficient detector performance of the X'tal cube (array-X'tal cube). Because we newly succeeded to fabricate the segmented crystal block by applying laser processing to a monolithic crystal, in this study, we evaluated performance of the X'tal cube using the monolithic crystal block (laser-X'tal cube). The results showed high crystal identification performance and average energy resolution of 8.6 % for all crystal segments, which are superior to the array-X'tal cube performance.

## 1. Introduction

The X'tal cube detector is a 3D position-sensitive radiation detector. Figure 1-a) illustrates structure of the X'tal cube. The X'tal cube is composed of a scintillation crystal block and a number of MPPCs optically coupled on all six surfaces of the block. The area between the MPPCs is covered with reflectors. The crystal block is segmented 3-dimensionally into cubes. There is no reflector between the crystal segments so that scintillation light is spread in the three directions and detected by the MPPCs at all six surfaces. The position where radiation has interacted inside the X'tal cube can be determined by identifying the crystal segment originating the scintillation light. For the determination, results of a simple Anger-type calculation that uses the signals of all MPPCs are represented in the 3D position histogram. Response of each crystal segment is formed in the histogram as shown in Figure 1-b), and accordingly, we can identify the radiation detected segments under the condition that each response is distinct.

The X'tal cube provides the same spatial resolution in the X, Y, and Z directions by the segmentation of the crystal block into cubes. The 3D information of the radiation detected location is useful in a PET detector application because it avoids causing parallax error which often degrades spatial resolution of PET images when the PET scanner has high sensitivity. The MPPC readout from all six crystal block surfaces is efficient because it does not require control of the light path. The readout also enables detection near the light originating position so that we can reduce attenuation of the light. In addition, the compactness of the

detector using MPPCs, thin photo-detectors, allows for a closely spaced assembly on a PET detector ring or a PET detector assembly in a rectangular geometry to gain a high detector packing fraction [1-3]. Because MPPCs are insensitive to magnetic fields, the X'tal cube can be also used in MR-PET systems which require a PET detector ring of small enough diameter to fit into the MR gantry [4].

Previously, we proved sufficient performance of the X'tal cube with the prototype using a 3D array of small cubic crystals for the crystal block (array-X'tal cube) [5]. In parallel with the study of the array-X'tal cube, we have developed crystal block fabrication technique by laser processing for easy and reliable assembly. We have confirmed feasibility of the technique with planer scintillators [6]. This time, we succeeded 3-dimensional segmentation of a monolithic crystal to fabricate the crystal block by applying the laser processing technique. In this study, we then evaluated performance of the X'tal cube using the segmented monolithic crystal (laser-X'tal cube).
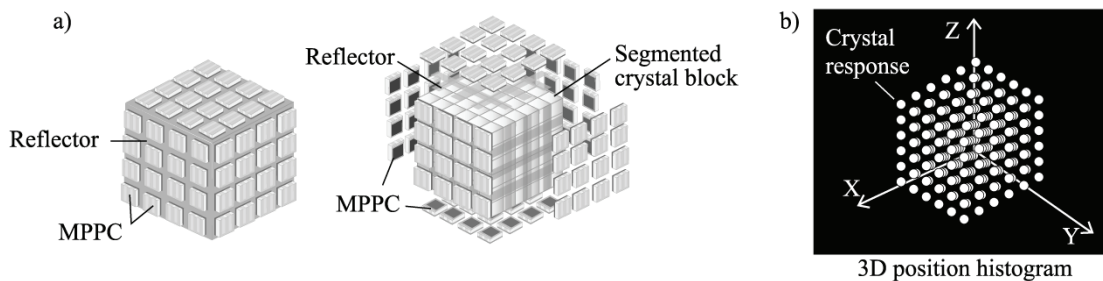


Figure 1. a) X'tal cube structure. b) 3D position histogram in which response of each crystal segment is appeared.

## 2. Methods

### 2.1 Materials

To study character of the laser-X'tal cube, its performance was compared with an array-X'tal cube. Figure 2-a) shows the crystal block of the laser-X'tal cube. An $18.0 \times 18.0 \times 18.0$ mm$^3$ monolithic LYSO crystal was segmented into $6 \times 6 \times 6$ of 3.0 mm cubic segments by the laser processing technique. It seems cloudy, however, its surface was mechanically polished. The crystal block for the array-X'tal cube was composed of a $6 \times 6 \times 6$ array of 3.0 mm cubic LGSO crystals. Figure 2-b) shows the crystal block. Surface of the LGSO crystals were chemically etched. Between crystal segments were remained as an air gap. For both X'tal cubes, we used the MPPCs of S10931-50P (Hamamatsu Photonics K.K., sensitive area; $3 \times 3$ mm$^2$, micro cell; 50 μm2, fill factor; 61.5 %). 96 MPPCs were arranged in six $4 \times 4$ arrays and coupled to all sides of the crystal block with RTV rubber (KE420, Shin-Etsu Chemical Co., Ltd., Japan, refractive index; 1.45). The reflector on the area between MPPC active areas was multilayer polymer mirrors (MPM) of 98% reflectivity and 0.065 mm thickness (Sumitomo 3M, Ltd., Japan) as reflector. Figure 2-c) indicates positions of MPPC active areas and crystal segments.
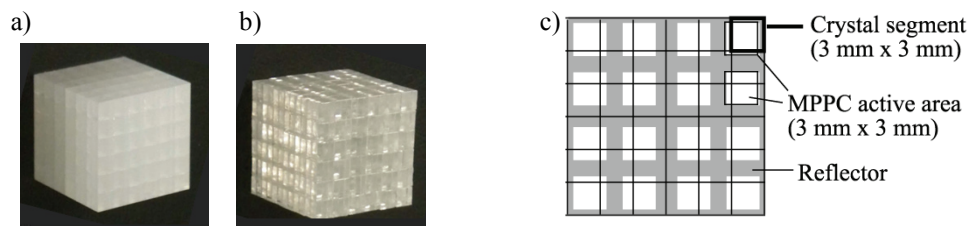
Figure 2. Crystal blocks of a) the laser-X'tal cube and b) the array-X'tal cube. c) Positions of 4 × 4 MPPC active areas and 6 × 6 crystal segments.

## 2.2 Experiments

To evaluate performance, 662 keV gamma-rays from ^{137}Cs were irradiated onto both of the X'tal cubes. To irradiate uniformly onto the detectors, some ^{137}Cs point sources were used. MPPC signals were acquired with a NIM and CAMAC based system. Because MPPC is very sensitive to temperature and bias voltage variation, the temperature was kept with ± 0.2 ℃ accuracy (standard deviation) in this study and the bias voltage for all MPPCs was set to 71.47 V. Results of Anger-type calculation with signals of all MPPCs were plotted on a 3D position histogram. Crystal identification performance was evaluated as discrimination of the crystal responses. Energy performance was done with summed signals of all MPPCs. As a further analysis to investigate X'tal cube character, light distribution among MPPCs were studied, which must reflect light spread inside the crystal block of each X'tal cube.

## 3. Results

Figures 3-a),b) show obtained 3D position histograms for the laser-X'tal cube and the array-X'tal cube, respectively. All crystal responses are distinct obviously. Figure 3 shows the crystal responses for a central and an outer 6 × 6 crystal segments extracted from the 3D position histograms (2D position histograms). They prove sufficient crystal identification performance of the both X'tal cubes. The responses distribute non-uniformly in the histograms for the array-X'tal cube.

Figure 4 shows pulse height distribution among MPPCs when an outer crystal segment, the colored crystal in the figure, detected radiations. The results indicate, in the crystal block of the laser-X'tal cube, scintillation light spreads only near the originating crystal segment. Meanwhile, in the array-X'tal cube, the light is considered to propagate along the crystal element lines because particularly large pulse heights are observed for the MPPCs at the ends of the crystal lines, indicated by thick arrows in the figure, even the MPPC on the most distant surface.

Figure 5 shows the pulse height distribution of the summed signals for each crystal segment: (a) a center and (b) a corner crystal segment for an outer 6 × 6 crystal segments and (c) a center and (b) a corner crystal segment for a center 6 × 6 crystal segments. The pulse heights show no considerable difference between the crystal segments for both the laser-X'tal cube and the array-X'tal cube. The relative light outputs and energy resolutions for the segments (a) - (d) are summarized in Table 1. We also measured energy resolutions for all 216 crystal segments. The average energy resolutions were (8.6 ± 0.4) % and (10.4 ± 0.6) % for the laser-X'tal cube and the array-X'tal cube, respectively.
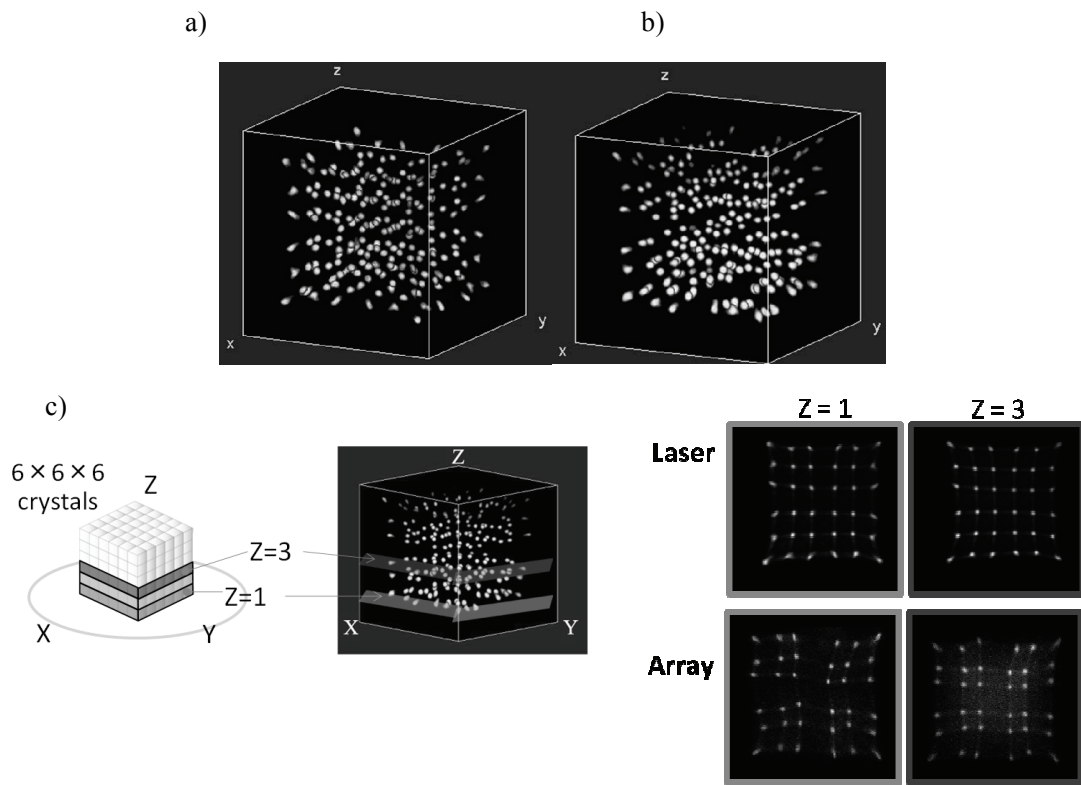
a)                                          b)



c)



Figure 3. a) 3D position histograms for the laser-X'tal cube and b) the array-X'tal cube. c) Crystal responses for a central (Z = 3) and an outer (Z = 1) 6 × 6 crystal segments (2D position histograms) extracted from the 3D position histograms in a) and b).
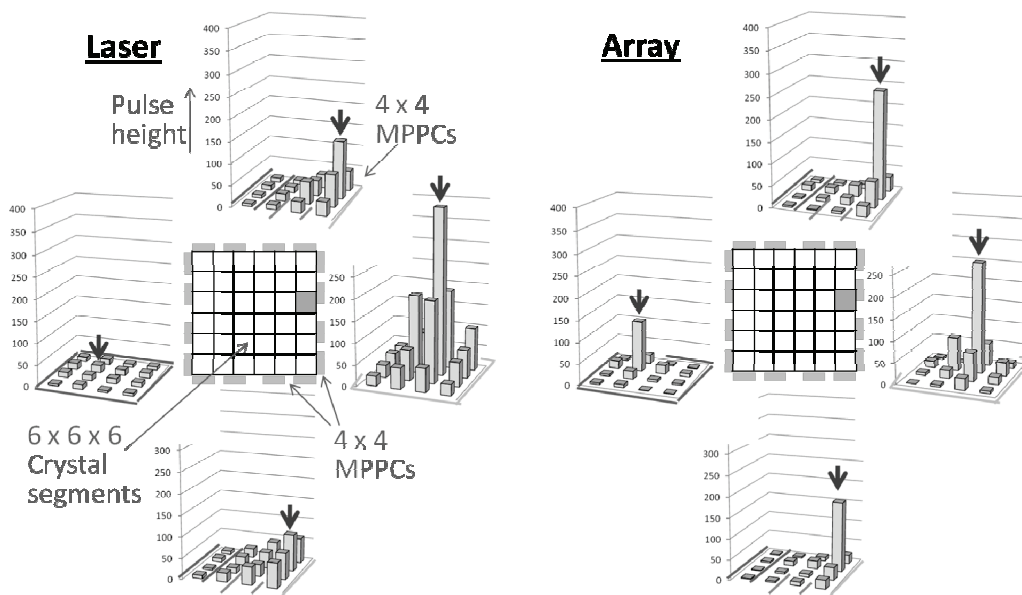


Figure 4. Pulse height distribution among MPPCs when an outer crystal segment (orange colored crystal) detected radiations. The red arrows indicate the MPPCs at the ends of the crystal lines including the outer crystal segment.
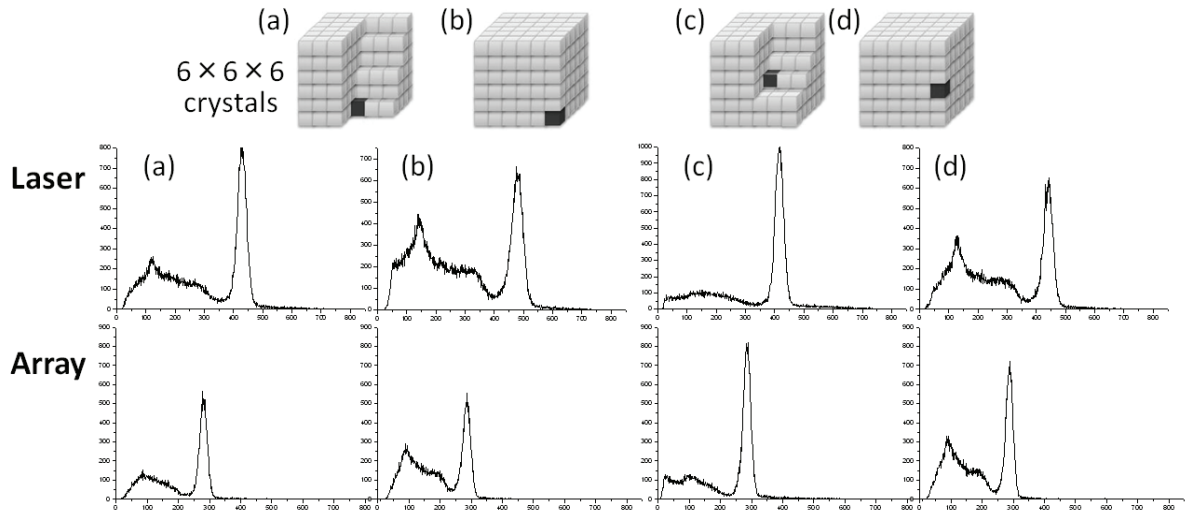
Figure 5. Pulse height distribution of the summed signals for each crystal segment: (a) a center and (b) a corner crystal segment for an outer 6 × 6 crystal segments and (c) a center and (b) a corner crystal segment for a center 6 × 6 crystal segments.

Table 1. Relative light outputs and energy resolutions of the crystal segments indicated in Figure 5.

| Laser-X'tal cube | (a) | (b) | (c) | (d) | Array-X'tal cube | (a) | (b) | (c) | (d) |
|---|---|---|---|---|---|---|---|---|---|
| Light output [a. u.] | 0.90 | 1.00 | 0.87 | 0.92 | Light output [a. u.] | 0.99 | 0.97 | 1.00 | 0.99 |
| Energy resolution [%] | 8.7 | 10.0 | 8.3 | 8.8 | Energy resolution [%] | 10.8 | 10.3 | 9.6 | 10.1 |

## 4. Discussion

As shown in Figure 3, both laser-X'tal cube and array-X'tal cube showed sufficient crystal identification performance in the condition of crystal segmentation into 3 mm cubic and using 96 MPPCs. However, non-uniform arrangement of crystal responses was observed in the position histogram of the array-X'tal cube. Because the non-uniform distribution will be disadvantage for finer crystal segments following larger number of crystal responses, we can conclude the laser-X'tal cube is superior to the array-X'tal cube in crystal identification performance.

The pulse height distributions among the MPPCs shown in Figure 4 indicated that light spread inside the crystal block is different between the two X'tal cubes. In the array-X'tal cube, light is considered to propagate along the crystal lines.

The laser-X'tal cube showed better energy resolutions than the array-X'tal cube as indicated in Figure 5 and Table 1. However, enough energy performance and no considerable position dependence are measured for both X'tal cube detectors.

## 5. Conclusions

We evaluated performance of the laser-X'tal cube newly developed by comparing the array-X'tal cube which has already proved its sufficient performance. From the results, we ensured that applying the laser processing technique to the crystal block was not only made the fabrication of the crystal block easier and more accurate but also improved detector performance of the X'tal cube.

## Acknowledgments

## References

[1]   J. Qi, C. Kuo, R. H. Huesman, G. J. Klein, W. W. Moses, and B. W. Reutter, "Comparison of rectangular and dual-planar positron emission mammography scanners", IEEE Trans. Nucl. Sci., Vol. 49, No. 5, pp. 2089-2096, 2002.

[2]   T. Kobayashi, T. Yamaya, H. Takahashi, K. Kitamura, T. Hasegawa, H. Murayama, and M. Suga, "A Monte Carlo simulation study on detector arrangement for a small bore DOI-PET scanner: jPET-RD", IEEE NSS MIC CR., M14-72, San Diego, California, 2006.

[3]   F. Habte, A. M. K. Foudray, P. D. Olcott, and C. S. Levin, "Effects of system geometry and other physical factors on photon sensitivity of high-resolution positron emission tomography", Phys.Med. Biol., 52, pp. 3753-3772, 2007.

[4]   C. Catana, Y. Wu, M. S. Judenhofer, J. Qi, B. J. Pichler and S. R. Cherry, "Simultaneous acquisition of multislice PET and MR images: initial results with a MR-compatible PET scanner", J. Nucl. Med. Vol. 47, pp. 1968–1976, 2006.

[5]   Yazaki Y, Murayama H, Inadama N, Osada H., Nishikido F, Shibuya K, Yamaya T, Yoshida E, Suga M., et al., The 'X'tal cube' PET detector: 3D scintillation photon detection of a 3D crystal array using MPPCs, Conf. Rec. NSS-MIC 2009, 3822–3826, 2009.

[6]   Moriya T, Fukumitsu K, Sakai T, Ohsuka S, Okamoto T, Takahashi H, Watanabe M, Yamashita T, Development of PET Detectors Using Monolithic Scintillation Crystals Processed With Sub-Surface Laser Engraving Technique, Nuclear Science, IEEE Transactions on 57(5), 2455–2459, 2010.

# Analog Signal Multiplexing Methods
# for SiPM Based Position Sensitive PET Block Detectors

Hyun Suk Yoon and Jae Sung Lee

Department of Nuclear Medicine, College of Medicine, Seoul National University, Korea

## Abstract

High-resolution preclinical positron emission tomography (PET) systems that consist of position sensitive block detectors are under development. This paper describes detector multiplexing techniques that simplify the extension of axial length or ring radius without employing extra data acquisition boards. Two analog multiplexing methods for SiPM based block detector were compared by assessing two block detectors with single data acquisition board (DAQ). By incorporating the multiplexing methods, flood image of two detector blocks was obtained with sing acquisition board. Although there was some degradation in spatial resolution compared to the one without multiplexing, individual crystals were clearly separated using one of the multiplexing methods.

## 1. Introduction

Positron emission tomography (PET) and PET/MRI systems dedicated for small animal and human breast are under development in our group (1-4). Such systems require high sensitivity for various reasons (5-8). Most efficient methods to improve the sensitivity of PET system would be the axial extension of detector rings by adding extra rings of block detectors. However, this extension requires additional power, cost and space consuming readout systems. On the other hand, we can effectively reduce the required readout systems by multiplexing the block detectors before digitizing the signals (Figure 1).
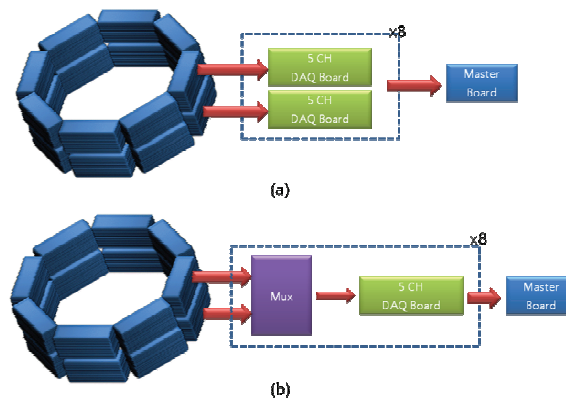


Figure 1. Two ring system without (a) and with axial multiplexing (b).

In this study, we tested two analog signal multiplexing methods shown in Figure 2 for SiPM based position sensitive PET block detectors. With this multiplexing technique, the readout of two block detectors will be possible without adding or changing the readout system.
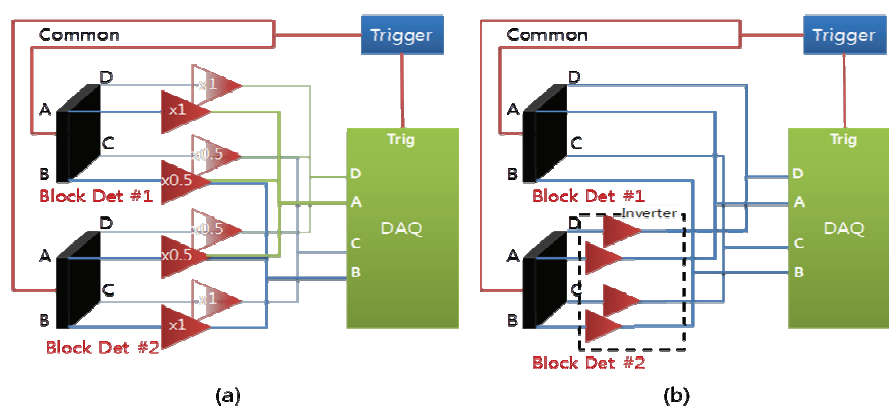
Figure 2. Simplified diagram of Spatial Multiplexing (a) and Bipolar Multiplexing (b) techniques

## 2. Methods

Each detector module used in this study is consists of $20 \times 18$ block array of $1.5 \times 1.5 \times 7$ mm$^3$ LGSO scintillation crystal, four SiPMs and charge division circuit to encode signals into 4 position related signals (14). FPGA based data acquisition system (DAQ) has 5 free-running 170 MSPS ADC to digitize 4 position dependent signals and a dynode signal. Each DAQ board receives signals from one block detector.

Two types of analog multiplexors were tested (Figure 2). One is spatially multiplexed, which uses 4 amplifiers that amplify 8 signals from two detectors with different gains that spatially separate two flood images. The gains were matched to maximize the dynamic range of position signals and to maintain energy information. The other type is bipolar multiplexing. The position dependant signals from one of the detectors were inverted while the others are not. The inverted and non-inverted signals were summed, and summed signals are used for obtaining energy and position information of events. The detector blocks are discriminated by applying zero energy thresholds (Figure 3). Shared common signal was used in both methods since the DAQ system only accepts single trigger. Flood images were acquired using both multiplexing methods and un-multiplexed detectors.

## 3. Results

Flood images were compared for both multiplexing methods and without multiplexor (Figure 4). In spatial multiplexing method, crystal peak arrays of two detector blocks were separated in a single flood image, but the width of crystal peaks were much shrunken in comparison to the one without multiplexing or bipolar multiplexor. Crystal peaks located at the edge were not clearly resolved.

On the other hand, the flood images of two detectors were clearly separated using the bipolar method. The crystal peaks were clearly resolved and the width of crystal peaks was slightly increased relative to the one without multiplexor.
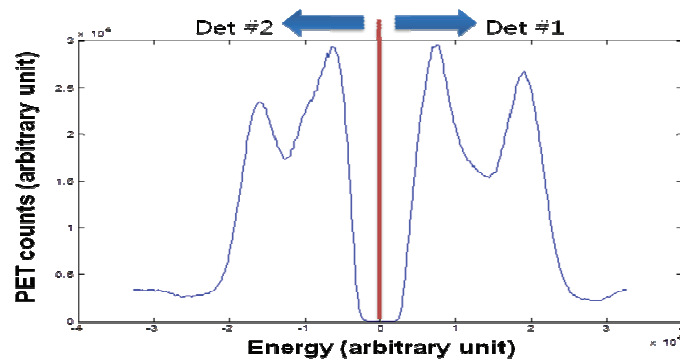
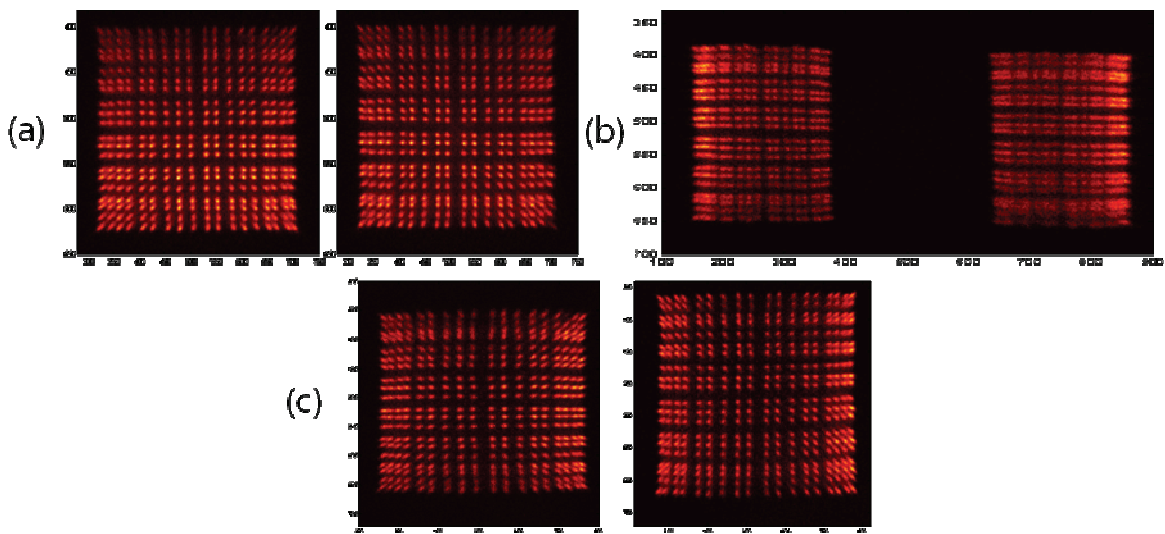Figure 3. Energy histogram of bipolar multiplexed detector.



Figure 4. Flood images of un-multiplexed (a), spatially multiplexed (b) and bipolar multiplexed (c) detector modules.

## 4. Discussion

Spatial multiplexing method shows degradation in flood images. The degradation would be caused by reduced dynamic ranges per block detector and increased input-referred noise. With the spatial multiplexing technique, each transmission line is connected to three outputs of the block detectors with different gains. Therefore, additional noise components would cause degradation of the flood images. However, bipolar multiplexing method shows the flood images with only slight change, which would be caused by the summation of the dark count noise from two block detectors instead of one.

## 5. Conclusions

Spatial and bipolar analog multiplexing techniques were verified through experiment. Applying these methods to the two ring PET system resulted in, 50% reduction in readout channels and 50% reduction in wire routing density. The bipolar multiplexing methods showed better results compared to the spatial multiplexor.

## References

[1]     S.I. Kwon, J.S. Lee, H.S. Yoon, et al., "Development of small-animal pet prototype using silicon photomultiplier (SiPM): initial results of phantom and animal imaging studies," *J Nucl Med.*, 52(4), pp.572-579, 2011.

[2]     S.J. Hong, I.C. Song, M. Ito, et al., "An investigation into the use of geiger-mode solid-state photomultipliers for simultaneous PET and MRI acquisition", IEEE Trans. Nucl Sci., 55(3), pp. 882-888, 2008.

[3]     J.S. Lee, S.J. Hong, "Geiger-mode avalanche photodiodes for PET/MRI. In: Iniewski K, eds. Electronic Circuits for Radiation Detection", CRC Press LLC, pp.179-200, 2010.

[4]     J.S. Lee, H.S. Yoon, G.B. Ko, et al., "Simultaneous PET/MR imaging with MR-compatible Geiger-mode APD PET system", IEEE Med Imaging Conf PET-MR Workshop, 2010.

[5]     Y.C. Tai and R. Laforest, "Instrumentation aspects of animal PET," *Annu. Rev. Biomed. Eng.*, 7, pp. 255–285, 2005.

[6]     M.G. Pomper and J.S Lee, "Small animal imaging in drug development," *Curr. Pharm. Des.*, 11, pp. 3247–3272, 2005.

[7]     M.V. Green, J. Seidel, J.J. Vaquero, et al,, "High resolution PET, SPECT and projection imaging in small animals," *Comput. Med. Imaging Graph.*, 25, pp. 79–86, 2001.

[8]     J.S. Kim, J.S. Lee, K.C. Im, et al., "Performance measurement of the microPET Focus 120," *J. Nucl. Med.*, 48( 9), pp.1527-1535, 2007.

[9]     S. Siegel, et al., "Simple charge division readouts for imaging scintillator arrays using a multi-chaneel PMT", IEEE Trans. Nucl. Sci. 43, pp.1634-1641, 1996.

[10]    V. Popov, "Analog readout system with charge division type output", Nuclear Science Symp. Conf. Record, pp. 1937-1940, 2001

[11]    V. Popov, S. Majewski and B.L. Welch, "A novel readout concept for multianode photomultiplier tubes with pad matrix anode layout", Nucl. Instrum. Methods Phys. Res. A 567, pp. 319-322, 2006

[12]    Olcott et al., "Compact readout electronics for position sensitive photomultiplier tubes", IEEE Trans. Nucl. Sci. 52, pp.21-27, 2005.

[13]    F.W.Y. Lau, A. Vandendroucke, P.D. Reynolds, et al., "Analog signal multiplexing for PSAPD-based PET detectors: simulation and experimental validation," Phys. Med. Biol., 55, pp. 7149-7174, 2010.

[14]    S.I. Kwon, S.J. Hong, M. Ito, et al., "Development of Position Encoding Circuit for a Multi-Anode Position Sensitive Photomultiplier Tube", Nucl. Med. Mol. Imaging, 42, no. 6, 2006.

# Development of DOI-PET detector integrated with RF coil for PET-MRI

Fumihiko Nishikido[1], Takayuki Obata[1], Naoko Inadama[1], Eiji Yoshida[1],
Mikio Suga[2] and Taiga Yamaya[1]

[1] National Institute of Radiological Sciences, Japan

[2] Chiba University

## Abstract

We are developing a new PET system integrated with an RF-coil of an MRI using a four-layer depth-of-interaction (DOI) detectors. In the proposed system, PET detectors which consist of a scintillator block, photo sensors and front-end circuits are placed close to the objective. Elements of the RF coil are inserted between gaps of the scintillation crystal block. Therefore the proposed system realizes high spatial resolution and sensitivity for the PET scanner by using the four-layer DOI detector. We constructed a prototype four-layer DOI-PET detector and carried out experiments in an actual MRI system to investigated influences on the PET detector and the MRI system from each other. As a result, sufficient detector performance of the DOI-PET detector regarding crystal identification and energy resolution was achieved in simultaneous measurements. The MRI images were also obtained as usual even though the DOI-PET detector was positioned close to the RF coil elements.

## 1. Introduction

Recently, various PET-MRI systems are being developed by a number of research groups. Since almost all the PET detectors for these PET-MRI systems have no depth-of-interaction (DOI) capability, the parallax error restricts their performances in studies for rodents and the human brain.

We are developing a PET scanner integrated with a birdcage RF coil for the PET-MRI system using a four-layer DOI detector we previously proposed [1]. A conceptual scheme of the proposed PET-MRI system is shown in Fig. 1. PET detectors which consist of a scintillator block, photo sensors and front-end circuits are placed close to the objective. Therefore the PET system of the proposed PET-MRI realizes high spatial resolution and sensitivity by using the four-layer DOI detector. The photo sensors and front-end circuits should be shielded to minimize noises from the MRI and influence on MRI imaging. If the shielding materials are inside the RF coils, the RF pulse is blocked by the shielding material and then a complete image cannot be obtained. To avoid the interference by the shielding material, each element of the RF coil is inserted between gaps of the scintillation crystal blocks. RF-coil element is positioned inside the shielding material. The closely-placed detector ring requires higher DOI capability, such as provided by the four-layer DOI encoding method, than conventional PET scanners.

We conducted a feasibility study for the PET detector integrated with the birdcage RF coil. We constructed a prototype four-layer DOI-PET detector and carried out experiments for performance evaluation in an actual 3.0 T MRI system. Additionally, we investigated influences on the DOI-PET detector and the MRI system from each other.
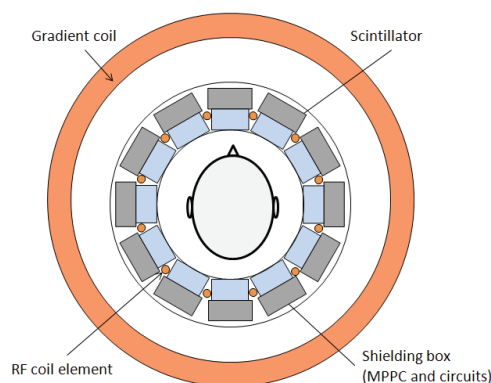
Figure 1.    Conceptual scheme of the proposed PET-MRI system

## 2.    Material and Methods

The prototype PET detector consisted of an LYSO crystal block and a $4 \times 4$ multi-pixel photon counter (MPPC) array (S11064 series, Hamamatsu Photonics K.K.). The size of each crystal element was 1.45 mm $\times$ 1.45 mm $\times$ 4.5 mm. The crystals were arranged in a $6 \times 6 \times 4$ layer with reflectors. Details of the reflector arrangement and the four-layer DOI encoding method are described in ref. [1]. Readout pixels of the MPPC are $3 \times 3$ mm$^3$ and they consist of the 50 μm cells. The detector and electrical circuit were packaged in an aluminum shielding box. Since they were located inside the MRI magnetic field, most circuit elements were made of nonmagnetic materials.

Experiments were carried out with 3.0 T MRI (GE, signa HDx) and a birdcage type RF-coil. The shielding box with the detector and circuit was mounted outside the RF-coil elements and inserted into the static magnetic field of the MRI. An electric power supply for the MPPC and a data acquisition system were outside the MRI room in order to reduce influence of electric noises on the MRI. The data acquisition system consisted of a trigger system, amplifiers and analog-to-digital converters (ADCs). The trigger signals were generated by summation of all the MPPC output signals and finally fed into the ADCs as gate signals. These systems were connected to the MPPC with 3 m long cables though a gap in a door to the MRI room.

Influences on the four-layer DOI PET detector from MRI were evaluated by comparing position histograms and energy spectra obtained for three experimental conditions. First, the DOI detector was positioned outside the MRI room for standard data. Second, the DOI detector was moved on the RF-coil without MRI measurement. Finally, simultaneous measurements with the DOI detector and the MRI were carried out. The MRI was operated in the gradient echo method during data acquisition of the DOI detector. In all the measurements, a $^{22}$Ns point-like source was positioned in the front of the DOI-PET detector. Acquisition time was 5 minutes in each measurement condition. Specified temperature control and correction of variance of the MPPC gains were not applied.

Next, the influence of the four-layer DOI PET detector on the MRI images was evaluated. A 13 cm diameter cylindrical phantom (CuSO$_4$ 5H$_2$O) was measured by the gradient echo method. First, a phantom image was obtained without the DOI detector. In this measurement, no DOI detector components were in

the MRI room and the door to the MRI room was closed. In the second measurement, the PET detector was mounted on the RF coil and the MPPC was turned off. Finally, the MPPC was turned on and simultaneous measurements were made with the PET detector and the MRI.

## 3. Results

Figures 2 shows position histograms for uniform irradiation of the $^{22}$Na point source. Only 511keV photo-peak events were indicated on these position maps. Each spot represents interacting events in certain crystal elements. The crystals in all four layers can be identified in all three position histograms. Comparison of the three position histograms shows no degradation of crystal identification performance by MRI measurement.
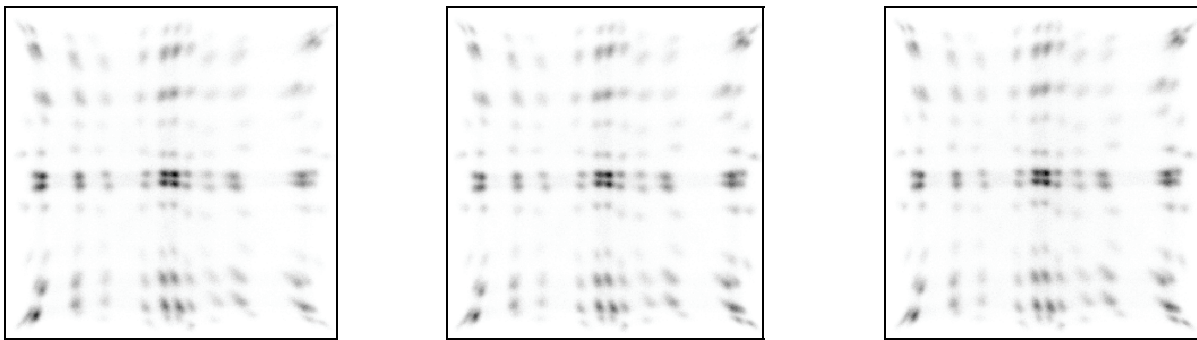


(a) Outside the MRI room     (b) On the RF-coil w/o MRI measurement     (c) Simultaneous measurement

Figure 2. Position histograms for uniform irradiation of 511 keV gamma rays for three experimental condition

Figures 3 show energy spectra for uniform irradiation of the $^{22}$Na point source. Ratios of the two photo-peak positions for each layer are ~2.4 which is nearly equal to the ratio of the gamma ray energies of 2.50 (=1.275/0.511). Linearity of the MPPC outputs to the gamma ray energy is enough to be used as the PET detector. Tables 1 and 2 summarize the photo-peak positions and energy resolutions for the 511 keV gamma rays. The photo-peak positions slightly decrease in the case of simultaneous measurements. On the other hand, differences in the energy resolution are within the margin of error. The degradation of the energy resolution in the fourth layer is mainly caused by internal Compton scattering. This degradation has been observed in another four-layer DOI detectors using MPPCs [2].
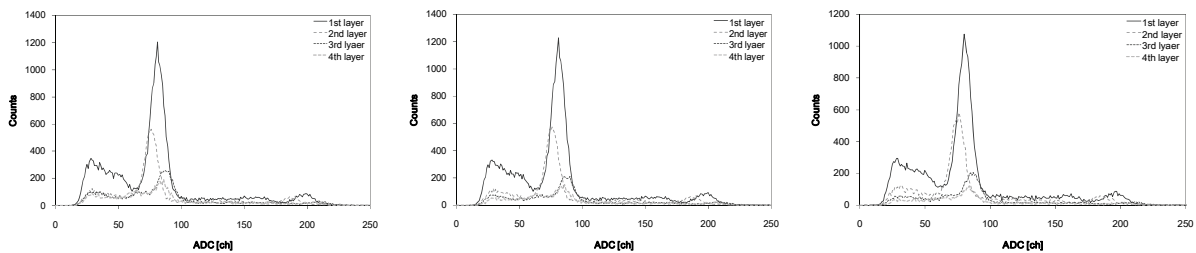


(a) Outside the MRI room     (b) On the RF-coil w/o MRI measurement     (c) Simultaneous measurement

Figure 3. Energy spectra for uniform irradiation of 511 keV gamma rays for three experimental conditions

Table 1. Photo peak positions (ch)

| layer | outside the MRI room | MRI off | MRI on |
|-------|---------|---------|--------|
| 1st | 82.1±0.2 | 82.0±0.2 | 81.3±0.2 |
| 2nd | 77.0±0.2 | 77.0±0.2 | 76.2±0.3 |
| 3rd | 88.2±0.3 | 88.4±0.3 | 87.2±0.4 |
| 4th | 85.3±0.9 | 85.5±0.9 | 84.0±1.2 |

Table 2. Energy resolutions (%, FWHM)

| layer | outside the MRI room | MRI off | MRI on |
|-------|---------|---------|--------|
| 1st | 16.4±0.7 | 15.9±0.7 | 16.1±0.6 |
| 2nd | 16.7±0.6 | 16.5±0.6 | 17.0±1.1 |
| 3rd | 17.3±1.0 | 16.4±1.1 | 17.2±1.1 |
| 4th | 17.6±2.6 | 17.7±2.7 | 19.6±3.0 |

Figure 4 shows an MRI image obtained in simultaneous measurements of the PET detector. Noises derived from the PET detector do not appear in Figs. 4 (b) and (c). These results show that shielding of the PET detector is satisfactorily even though the PET detectors are close to the RF coil.
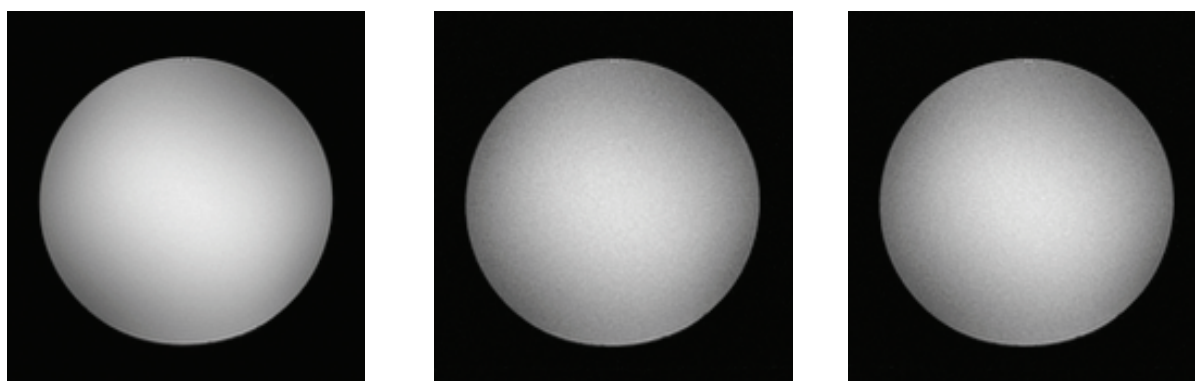


(a) Without the PET detect    (b) With the PET detector (MPPC turned off)    (c) Simultaneous measurement

Figure 4. MRI images in the case of various dummy detector positions.

## 4. Conclusions

We proposed the new system with integrated PET detectors and the birdcage type RF coil for the PET-MRI. This system realizes high spatial resolution and sensitivity for the PET scanner by using the four-layer DOI detector. We constructed and tested the prototype four-layer DOI-PET detector for the PET-MRI system. The DOI-PET detector was successfully demonstrated to work normally in simultaneous measurements of MRI. The MRI images were also obtained as usual even though the PET detector was positioned close to the RF coil

## References

[1]    T. Tsuda, H. Murayama, K. Kitamura, et al., "A Four-Layer Depth of Interaction Detector Block for Small Animal PET", IEEE Trans. Nucl. Sci., vol. 51, No. 5, pp. 2537-2542, Oct., 2004

[2]    F. Nishikido, T. Mitsuhashi, N. Inadama, E. Yoshida, H. Murayama, T. Yamaya,"Performance Evaluation of Four-Layer DOI Detectors Using Multi-Pixel Photon Counter Arrays", Conference record of 2010 IEEE Nuc. Sci. Sympo. & Med. Imag. Conf. Record., M14-58, 2008.,

# Development of SiPM PET combined with 9.4 T animal-dedicated MRI

Guen Bae Ko[1], Hyun Suk Yoon[1], Sun Il Kwon[1], In Chan Song[3], Seong Jong Hong[2],
and Jae Sung Lee[1]

[1] Department of Nuclear Medicine, Seoul National University, Seoul, South Korea

[2] Department of Radiological Science, Eulji University, Gyeonggi-do, South Korea

[3] Department of Radiology, Seoul National University, Seoul, South Korea

## Abstract

PET/MRI is powerful imaging modality for clinical and preclinical study because it provides functional and anatomical information simultaneously. In this talk, we will present the proposed design of our next generation SiPM PET detector and plans for combination with 9.4 T animal-dedicated MRI. The results of Monte Carlo simulation to predict system characteristics will be presented.

## 1. Introduction

Positron emission tomography (PET) is a biomedical imaging modality that provides functional and biochemical information of body with high sensitivity. However, since PET provides limited anatomic information, lots of efforts have been put into combined PET with anatomical imaging systems. Combining PET with MRI has several advantages than integrating PET with CT. Relative to CT, MRI has low radiation dose and high soft tissue contrast. Furthermore, MRI can provide other useful information rather than anatomy: MR spectroscopy (MRS) and functional MRI (fMRI).

The progress of simultaneous PET/MRI technologies has been accelerated by recent developments of solid state photo-sensor, such as avalanche photo-diode (APD) and silicon photomultiplier (SiPM) [1-4]. These semiconductor devices are suitable for animal-dedicated PET/MR systems because of its magnetic-field insensitivity and compact size.

Our group has developed SiPM-based PET systems with the ultimate goal of preclinical and clinical simultaneous PET/MR imaging [4, 5]. Here, we'd like to introduce the design concept of our next generation SiPM-based PET system that will be combined with 9.4 T animal-dedicated MRI. The basic physical characteristics of this system predicted by Monte Carlo simulation will be also described. This PET/MR system would be useful multimodal imaging tool for preclinical researches including neurotransmitters, cell tracking, and various metabolism studies [6].

## 2. Methods

### 2.1 SiPM PET detector design

The detector that we have designed consists of $11 \times 50$ LYSO crystal array and four ($1 \times 4$ array) SiPMs with 16 output channels (S11828-3344M; Hamamatsu, Japan) as illustrated figure 1. Each LYSO pixel has the dimension of $1.0 \times 1.0 \times 10 \text{ mm}^3$. This block will be mounted on the resistive charge division network

(RCN) for signal multiplexing. Because of the temperature dependent gain change of SiPM, bias voltage control system will be also implemented.
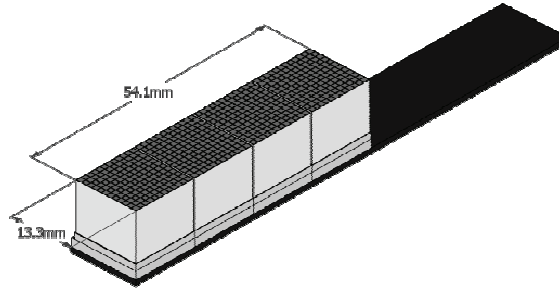


Figure 1. Design of SiPM PET detector

## 2.2 Plan for combination with animal-dedicated MRI

In this project, we focus on the combination of a high-resolution SiPM PET scanner with a 9.4 T animal-dedicated MRI (Agilent, USA) system for preclinical research. The SiPM PET will be inserted between gradient and RF coils as done in previous studies with APD-based PET inserts (Figure 2). The inner diameter of gradient coil is 100 mm and the outer diameter of millipedes RF coil is 60 mm.
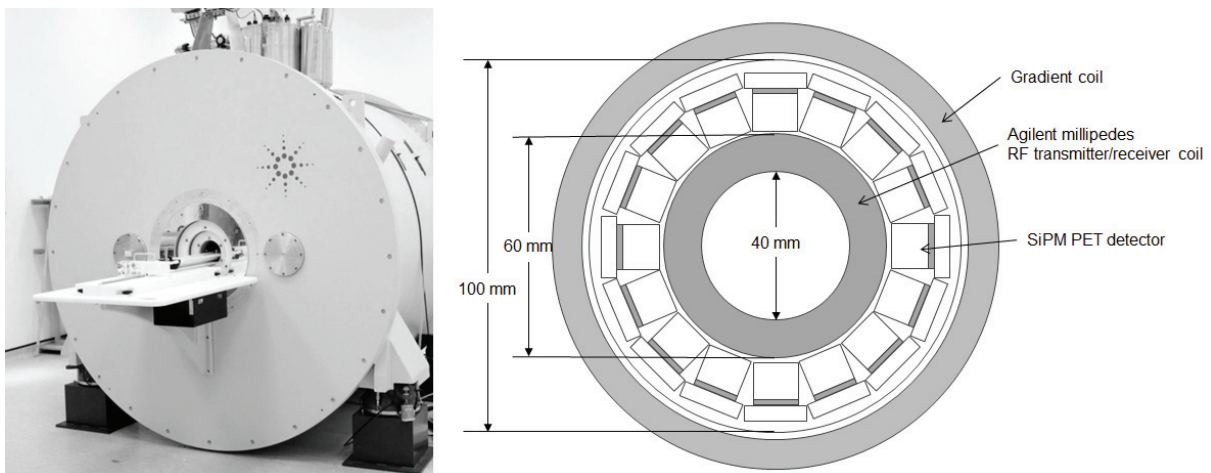


Figure 2. Agilent 9.4 T MRI (left) and SiPM PET inserts combined with animal-dedicated MRI (right).

Careful shielding of PET detector module will be required because the radio frequency (RF) signals of MRI and electrical noise due to PET electronics significantly affect the performance of PET and MRI mutually.

## 2.3 Monte Carlo simulation

To predict the performance of PET system, Monte Carlo simulation was performed using GATE simulation toolkit. In the simulations, back-to-back 511 keV gamma-rays were emitted. Figure 3 shows the

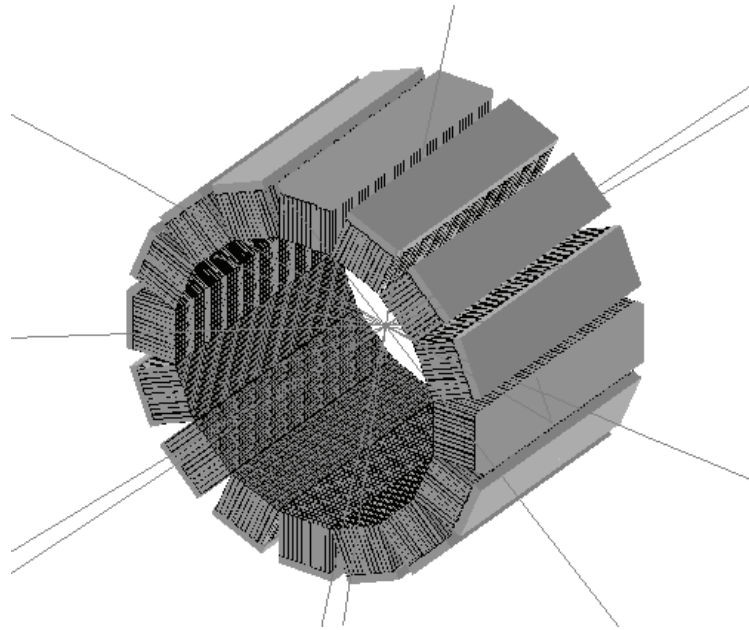simulation condition, in which 16 PET detector modules were employed.



Figure 3. Monte Carlo simulation of proposed SiPM PET insert.

## 3. Results

The PET inserts has 54 mm axial field-of-view (FOV). The maximum sensitivity at each energy window was 7.0%, 5.5%, and 5.3% for energy windows of 250-750, 350-650, and 400-600 keV, respectively (Figure 3).
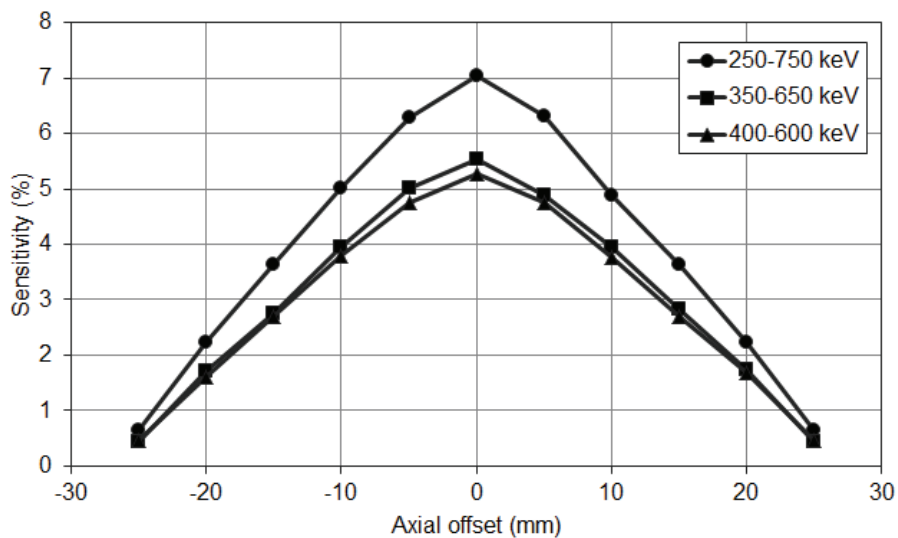


Figure 3.Sensitivity values measured at various axial offsets.

## 4. Discussion & Conclusions

Design of SiPM PET that will be integrated with 9.4 T animal-dedicated MRI is proposed and Monte Carlo simulation was performed. This PET/MR system will be useful preclinical research tool because it has good sensitivity and large FOV.

## References

[1]    C. Catana, Y. B. Wu, M. S. Judenhofer et al., "Simultaneous acquisition of multislice PET and MR images: Initial results with a MR-compatible PET scanner," *J. Nucl. Med.*, vol. 47, no. 12, pp. 1968-1976, Dec, 2006.

[2]    M. S. Judenhofer, H. F. Wehrl, D. F. Newport et al., "Simultaneous PET-MRI: a new approach for functional and morphological imaging," *Nat. Med.*, vol. 14, no. 4, pp. 459-465, Apr, 2008.

[3]    S. Yamamoto, M. Imaizumi, Y. Kanai et al., "Design and performance from an integrated PET/MRI system for small animals," *Ann. Nucl. Med.*, vol. 24, no. 2, pp. 89-98, Feb, 2010.

[4]    S. I. Kwon, J. S. Lee, H. S. Yoon et al., "Development of Small-Animal PET Prototype Using Silicon Photomultiplier (SiPM): Initial Results of Phantom and Animal Imaging Studies," *J. Nucl. Med.*, vol. 52, no. 4, pp. 572-579, Apr, 2011.

[5]    H. S. Yoon, G. B. Ko, S. I. Kwon et al., "Simultaneous PET/MRI with an MR-compatible silicon photomultiplier (SiPM) PET scanner," *J. Nucl. Med.* [In press]

[6]    H. F. Wehrl, M. S. Judenhofer, S. Wiehr et al., "Pre-clinical PET/MR: technological advances and new perspectives in biomedical research," *Eur. J. Nucl. Med. Mol. Imaging*, vol. 36 Suppl 1, pp. S56-68, Mar, 2009.

# Development of the small OpenPET prototype
# and its real-time imaging system

Hideaki Tashima[1], Eiji Yoshida[1], Shoko Kinouchi[2,1], Mikio Suga[2], Hideaki Haneishi[3]
and Taiga Yamaya[1]

[1] Molecular Imaging Center, National Institute of Radiological Sciences, Japan

[2] Graduate School of Engineering, Chiba University , Japan

[3] Research Center for Frontier Medical Engineering, Chiba University, Japan

## Abstract

The OpenPET and its real-time imaging capability have great potential for real-time tumor tracking in medical procedures such as biopsy and radiation therapy in addition to the real-time monitoring of the dose distribution during particle therapy. For the real-time imaging system, we intend to use the one-pass list-mode dynamic row-action maximum likelihood algorithm (DRAMA) and implement it using general-purpose computing on graphics units (GPGPU) techniques. However, it is difficult to make consistent reconstructions in real-time because the amount of list-mode data acquired in PET scans may be large depending on the level of radioactivity in the field of view, and the reconstruction speed depends on the amount of the list-mode data. In this study, we developed a system to control the data used in the reconstruction step while retaining quantitative performance. In the proposed system, the data transfer control system limits the event counts to be used in the reconstruction step according to the reconstruction speed, and the reconstructed images are properly intensified by using the ratio of the used counts and the total counts. We implemented the system on the small OpenPET prototype and evaluated the performance in terms of the real-time tracking ability by displaying reconstructed images in which the intensity was compensated. The intensity of the displayed images correlated properly with the original count rate and a frame rate of 2 frames per second was achieved with average delay time of 2.1s.

## 1. Introduction

We have proposed the OpenPET, an open type positron emission tomography (PET) having a ring gap between two detector rings, which allows easy access to the patient during PET scanning[1]. The OpenPET has mainly three types of possible applications: 1) integration of treatment and diagnosis; 2) simultaneous multimodal imaging; and 3) entire-body PET with a limited number of detector rings. The first item includes the in-beam PET for monitoring dose distribution *in situ* during particle therapy[2,3] and real-time tumor tracking for PET-guided medical procedures such as biopsy and radiotherapy. It should be noted that tumor-tracking is a much more challenging application in terms of the real-time requirement. The second item includes PET-CT that can image the same field of view (FOV) at exactly the same time by inserting the x-ray CT system into the gap. The third item is the extension of the FOV. The OpenPET with two detector rings of an axial length $W$ can extend the axial FOV to $3W$. For a proof-of-concept of the OpenPET,

we developed a small OpenPET prototype (Figure 1), which has two detector rings (110 mm diameter and 42 mm axial length) composed of eight block-detectors[4]. Each block-detector has 14×14×4 LGSO crystals. Although the OpenPET imaging of the in-gap area uses only oblique lines of response (LORs), the depth-of-interaction detector suppresses the spatial resolution deterioration in the FOV. For real-time imaging of the OpenPET, we intend to use the recently developed fast PET reconstruction algorithm, one-pass list-mode dynamic row-action maximum likelihood algorithm (DRAMA)[5], and general-purpose computing on graphics processing units (GPGPU) techniques[6]. GPGPU techniques can significantly reduce the computational time. However, it is still difficult to achieve real-time visualization if the amount of list-mode data is huge for the real-time processing. In this study, we propose a system architecture to control the amount of data to be processed for real-time reconstruction. We implement the architecture on the small OpenPET prototype and evaluate the performance in terms of real-time processing ability.
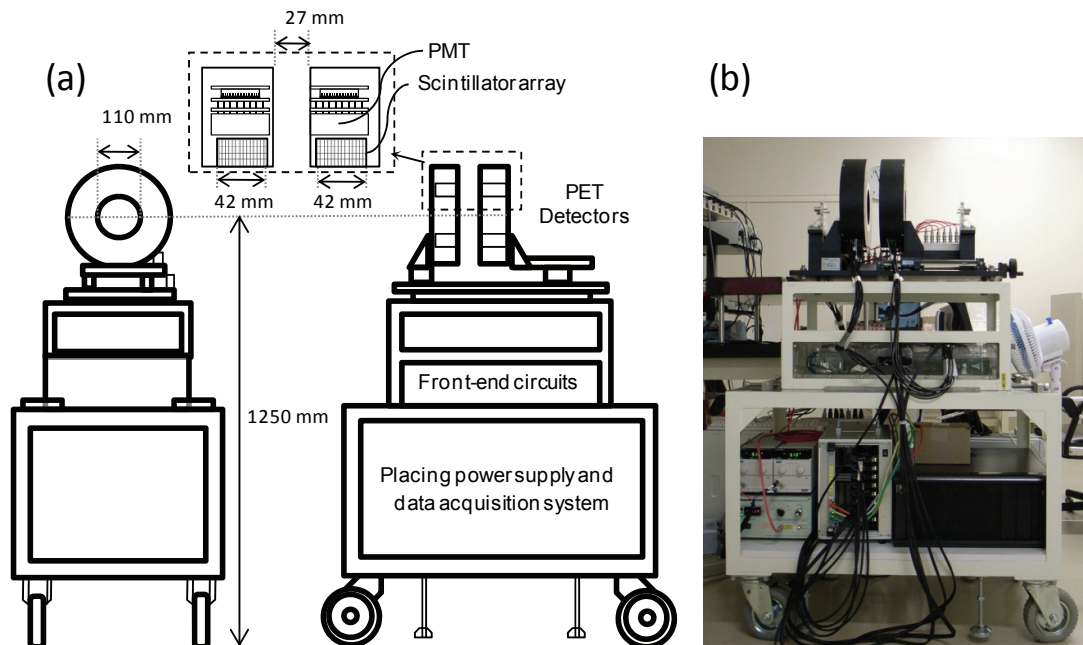


Figure 1. Small OpenPET prototype: (a) schematic design and (b) photograph.

## 2. Methods

### 2.1 Architecture

The OpenPET system detects coincidence gamma ray event data, converts them into a list-mode data file format and places them in storage. Conventionally, images are reconstructed after all data are acquired. To perform real-time imaging, we propose a system architecture without large changes from the current system design. Figure 2 shows the basic concept of the proposed system architecture of the real-time imaging system for the OpenPET. The data transfer control system transfers a part or all of the list-mode data acquired by the OpenPET to be used by the real-time reconstruction system according to the processing capacity of the real-time reconstruction system. After reconstruction is done, the image intensity is compensated according to the transfer ratio. Then the real-time viewer system displays the image on the PC screen.
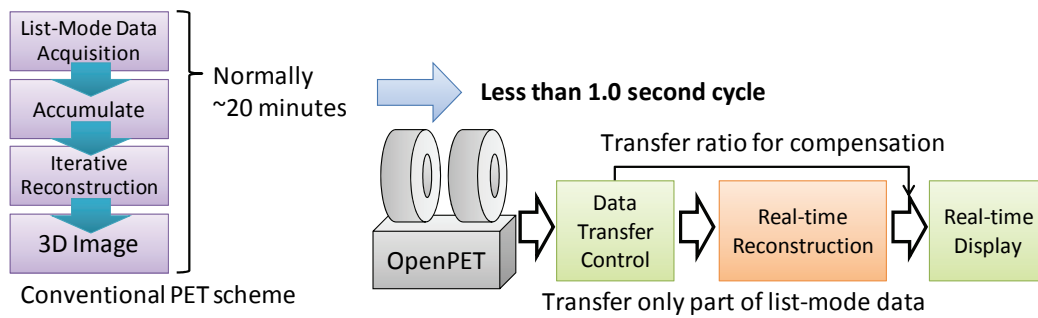
Figure 2. Basic concept of the proposed system architecture.

## 2.2 Implementation

We implemented the real-time viewer, data transfer control and real-time reconstruction systems on a single PC having 3.33 GHz Intel® Core™ i7 CPU, 24 GB memory (2.5 GB for system memory and 21.5 GB for RAM disk) and a NVIDIA® Tesla® C1060 graphics processing unit (GPU) card, which was connected to the small OpenPET prototype. In our implementation, these systems worked independently and transferred the data among them by using the RAM disk. The real-time reconstruction system was implemented with the one-pass list-mode DRAMA using GPGPU techniques on compute unified device architecture (CUDA) version 2.3.

## 2.3 Experiments

The system performance in terms of the real-time tracking ability was demonstrated by a point source tracking experiment. In the demonstration, a $^{22}$Na point source (1MBq) was put on a moving stage with a long bar so that the source was placed between the gap of the small OpenPET prototype (Figure 3). The number of counts to be used in the GPU-implemented list-mode DRAMA was limited below 5,000 and voxel size was set to $3.0 \times 3.0 \times 3.0$ mm$^3$ for better frame rate performance. The reconstructed image size was $38 \times 38 \times 42$ voxels.
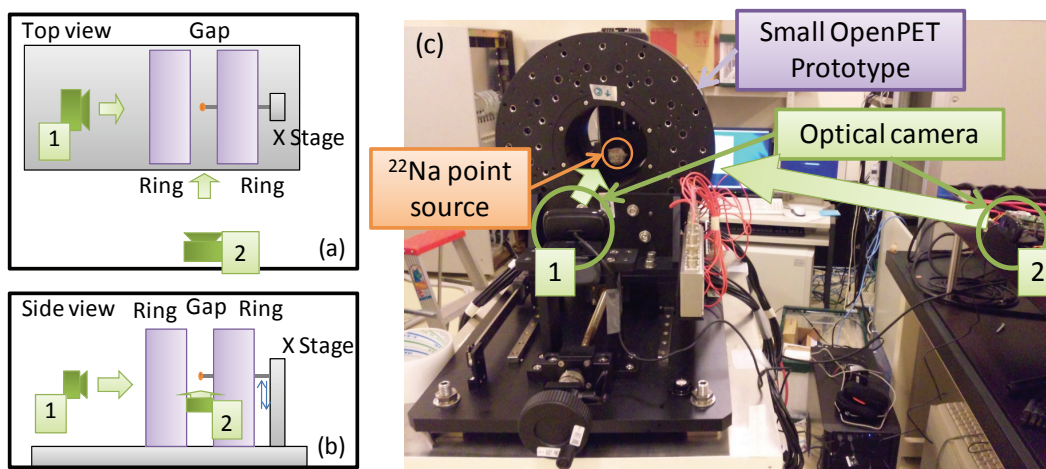


Figure 3. Tracking ability demonstration setup: (a), (b) schematic illustration of top and side view, (c) photograph of the demonstration setup. $^{22}$Na point source (1 MBq) was set between the ring gap and moved up and down with a 30 s or 20 s cycle.

## 3. Results

In the demonstration we displayed transaxial, coronal and sagittal slices of the reconstructed OpenPET images and movies of a moving point source captured by optical cameras on the PC screen simultaneously (Figure 4). The point source moved up and down with a 30 s or 20 s cycle sine curve and the real-time viewer showed the reconstructed images with a frame rate of 2 frames per second (fps). Figure. 5 shows displayed point source position on the screen. From the sine curve fitting, an average delay time of 2.1 s was obtained and the mean errors were 2.0 mm for 30 s cycle and 3.3 mm for 20 s cycle.
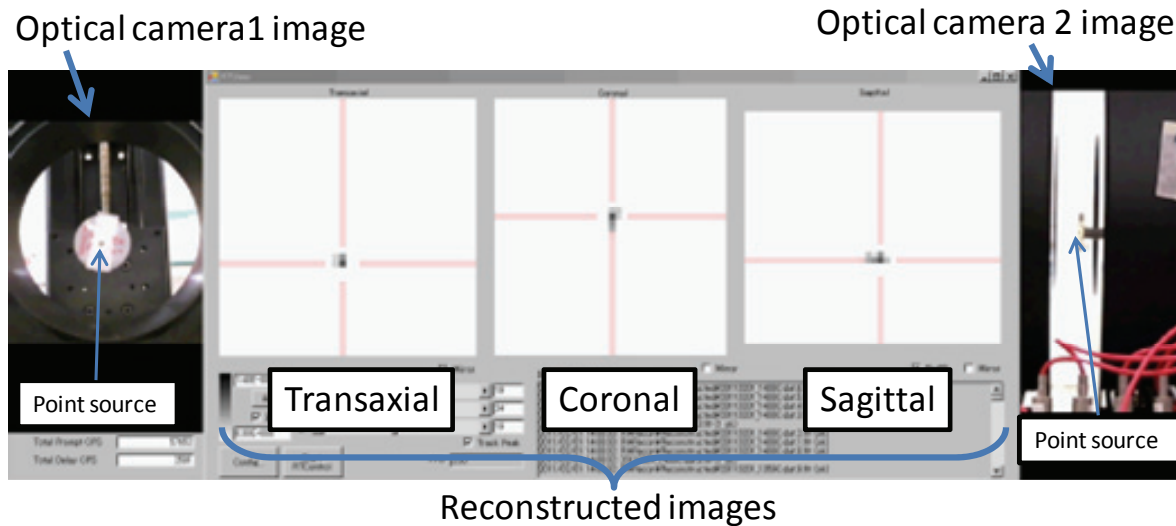


Figure 4. Example of images captured during the tracking demonstration. Optical camera images are shown with reconstructed images in which slices containing the maximum-valued voxel were selected. Actual frame rate was 2 fps in the demonstration.
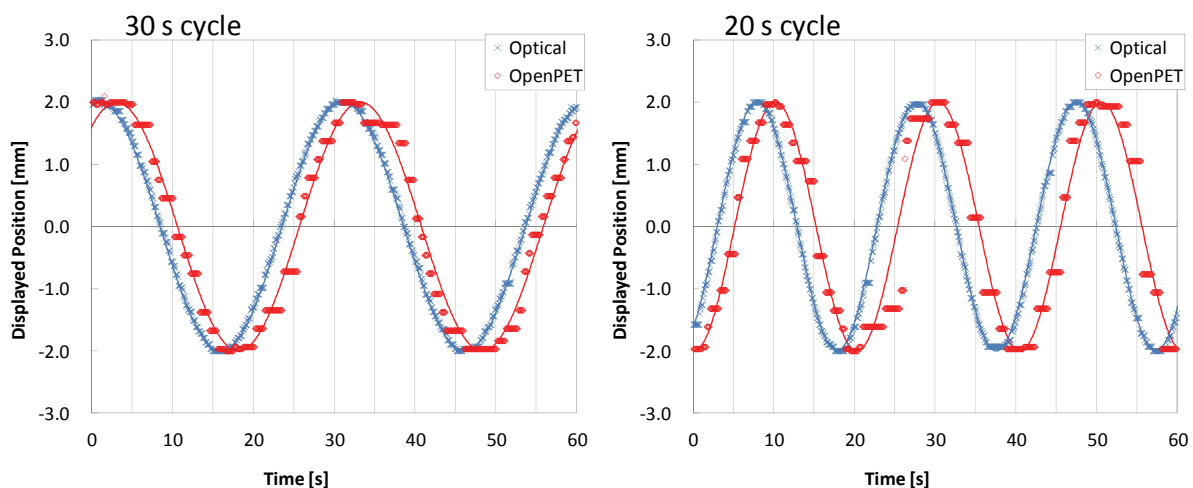


Figure 5. Displayed positions of the point source in the images obtained by the optical camera and by the OpenPET during the tracking demonstration (left: 30 s cycle, right 20 s cycle). From the sine curve fitting, the delay was determined as 2.1 s in both cases.

## 4. Discussion

We expected that the main bottlenecks in the real-time imaging system were reconstruction speed and stability. The proposed architecture resolved them by introducing the real-time reconstruction system and data transfer control systems. The reconstruction speed was accelerated by using the one-pass list-mode DRAMA and its GPU implementation, and it was stabilized by the data transfer control system which controls maximum data usage. Other expected bottlenecks were communication speed among systems. The communication speed was accelerated by implementing them on the same computer and using the RAM disk. The random access performance of the RAM disk was 40-100 times faster than a conventional hard disk drive. However, the evaluation of the delay showed that the total delay of the current system was 2.1 s. The clear breakdown of the delay was 0.5 s for data accumulation and 0.5 s for reconstruction and the rest could not be analyzed yet. We expect that it includes delay in the data acquisition system, which we plan to improve in the next version of the OpenPET prototype.

## 5. Conclusions

We proposed the system architecture for the real-time imaging system of the small OpenPET prototype. The point source tracking demonstration showed that the system has a good possibility for real-time tumor tracking while maintaining quantitative accuracy.

## Acknowledgments

## References

[1]    T. Yamaya, T. Inaniwa, S. Minohara, et al., "A proposal of an open PET geometry," *Phys. Med. Biol.*, vol. 53, pp. 757-73, Jan. 2008.

[2]    Y. Iseki, T. Kanai, M. Kanazawa, et al., "Range verification system using positron emitting beams for heavy-ion radiotherapy," *Phys. Med. Biol.*, vol. 49, July 2004, pp. 3179-95.

[3]    T. Nishio, T. Ogino, K. Nomura, and H. Uchida, "Dose-volume delivery guided proton therapy using beam on-line PET system," *Med. Phys.*, vol. 33, Oct. 2006, pp. 4190-7.

[4]    T. Yamaya, E. Yoshida, T. Inaniwa, et al., "Development of a small prototype for a proof-of-concept of OpenPET imaging," Phys. Med. Biol., vol. 56, Jan. 2011, pp. 1123-37.

[5]    T. Nakayama and H. Kudo, "Derivation and implementation of ordered-subsets algorithms for list-mode PET data," *IEEE Nucl. Sci. Symp. Conf. Rec.*, Oct. 23-29, 2005, pp. 1950-4.

[6]    S. Kinouchi, T. Yamaya, E. Yoshida, et al., "GPU implementation of list-mode DRAMA for real-time OpenPET image reconstruction," *IEEE Med. Imag. Conf.*, Oct. 30 - Nov. 6, 2010, M09-281.

# Accelerated Shift-Variant Resolution Recovery Reconstruction for Compton Camera

Soo Mee Kim[1], Hee Seo[2], Jin Hyung Park[2],
Chan Hyeong Kim[2], Dong Soo Lee[1], Jae Sung Lee[1]

[1] Department of Nuclear Medicine, Seoul National University, Korea

[2] Department of Nuclear Engineering, Hanyang University, Korea

## Abstract

In this study, the shift-variant point spread function (SV-PSF) for the Compton camera is expressed by the measurements of various point sources in FOV and it is incorporated into the system matrix of fully three-dimensional and accelerated reconstruction, i.e. listmode OSEM (LMOSEM) algorithm, for resolution recovery. The simulation data of the point sources were used to estimate shift-variant parameters of three different PSF models, Gaussian, Cauchy, and general parametric function. Although there was no much difference between the fitness of Gaussian and general parametric models, the general parametric model showed more flexibility dependent on the distance from the Compton camera than Gaussian model. LMOSEMs with SV-PSF of 2 point sources yielded more improved resolution over the FOV than LMOSEMs without PSF and with shift invariant PSF.

## 1. Introduction

The conventional Compton camera consisted of two detectors; the scatterer detector and the absorber detector. The detection process can be expressed mathematically by surface integration of a cone which is defined by two detection positions and a scattering angle of each recorded event. As shown in Figure 1, the spatial resolution of the Compton camera suffers from the uncertainties of detection positions and energies measured from the scatter and absorber detectors[1]. Moreover, the degradation degree of the spatial resolution is different over field-of-view (FOV).
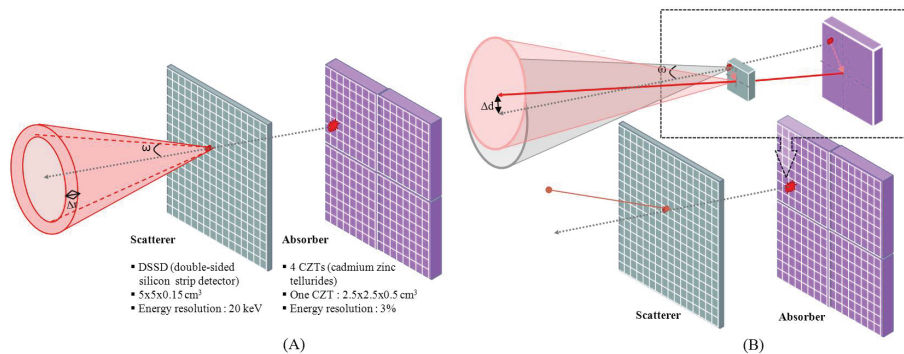


Figure 1. (A) Angular ($\Delta r$) and (B) positional measurement uncertainties ($\Delta d$) in a Compton camera.

In this talk, we will present a measurement strategy and three different models (Gaussian, Cauchy, and

general parametric models) for the shift-variant point spread function (SV-PSF). In addition, the estimated SV-PSF is incorporated into the accelerated statistical reconstruction, i.e. listmode ordered subset expectation maximization (LMOSEM), for resolution recovery.

## 2. Methods

We considered three models; Cauchy (Eq. (1)), Gaussian (Eq. (2)), and general parametric model (Eq. (3))[2], to express the shift-variant point spread function (SV-PSF). *A* and *b* are the height and location of the peak of each function, respectively and *c* controls the width of the function.
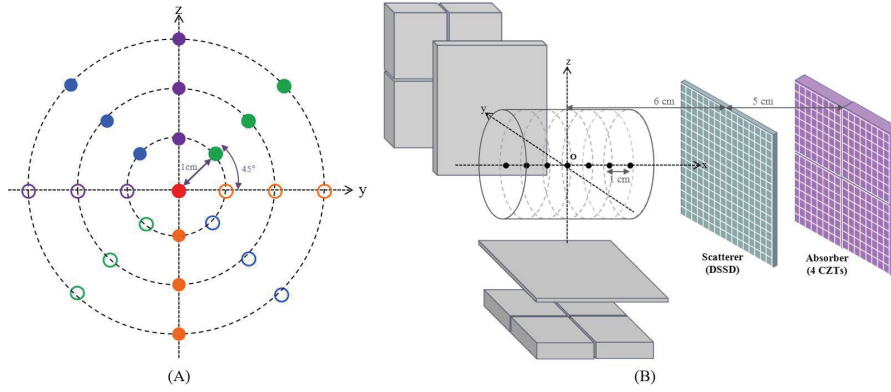


Figure 2. The placement strategy of point sources for SV-PSF measurements over FOV; (A) point sources located at different radii and polar angles on the yz plane; (B) the successive yz-plane measurements at different distances from scatterer detector on the x-axis in three Compton cameras.

The parametric model in Eq. (3) has a general form between Cauchy and Gaussian functions by the parameter of $\gamma$. When $\gamma$ equals to 1, it becomes the Cauchy function; when $\gamma$ goes to infinite value, it reaches the Gaussian function.

$$PSF_i(x) = A(i) \cdot \exp\left[-\left(\frac{x - b(i)}{c(i)}\right)^2\right] \quad (1)$$

$$PSF_i(x) = A(i) \cdot \left[\frac{c^2(i)}{\left(x - b(i)\right)^2 + c^2(i)}\right] \quad (2)$$

$$PSF_i(x) = A(i) \cdot \left[1 + \frac{(x - b(i))^2}{\gamma(i)c^2(i)}\right]^{-\gamma(i)} \quad (3)$$

$$\hat{f}_i^{k+1,l+1} = \frac{\hat{f}_i^{k,l}}{S_i \otimes G_i}\left\{\sum_{j \in \{mn\omega\}} \frac{H_{i;j}}{\sum_p \left(\hat{f}_p^{k,l} \otimes G_p\right) H_{p;j}}\right\} \otimes G_i \quad (4)$$

The point sources were placed and measured at different radii and different polar angles on the yz-plane as shown in Figure 2(A). The PSF corresponding to the blank points were assumed to be the same as those colored solid points by the rotation-based symmetric relationship. The same measurement on the yz-plane was repeated at the different distances from the Compton camera on the x-axis (Figure 2(B)). The parameters (*A*, *b*, *c*, and $\gamma$) of PSF functions were fitted separately on the x, y, z-profiles of the

reconstructed images using nonlinear least-squares.

For resolution recovery, we incorporated the fitted PSFs into the system model of LMOSEM algorithm as shown in Eq. (4). The 3D PSF ($G_i$) at $i$th voxel was calculated by the products of the normalized PSFs of x, y, z axes and was employed in forward and backward projection processes using image-space convolution operation which is suggested in *Ref.* [3] for resolution recovery. The function parameters at the given voxel were derived from measurements of point sources by piecewise linear interpolation.

## 3. Results

At the closer distance from the Compton camera, the larger gamma value was estimated. It implies that the PSF shape is similar to Gaussian function at a close distance. This shape changed to the Cauchy function when the distance is longer. Figure 3 shows that the Cauchy function resulted in broad histogram of the sum of the squared 2-norm of the residual (SSR) which is a difference between the measured profile and the fitted curve. The general parametric model provided the narrowest and smallest SSR, but it was not much different from the Gaussian function.

The performance of LMOSEM with Gaussian SV-PSF was compared with shift-invariant PSF (SIV-PSF) using combined MC data of two point sources which were located by 4 cm apart from each other at different distances on the x axis. The simplest reconstruction approach, simple backprojection (SBP) in Figure 4(A) gave limited spatial resolution. In comparison with SBP, LMOSEM without PSF model (Figure 4(B)) provided better SNR, but still insufficient spatial resolution. Both LMOSEM with Gaussian (C) SIV and (D) SV-PSF provided more improved spatial resolution of the reconstructed images than LMOSEM without PSF (B). Compared to SIV-PSF-LMOSEM, the two point sources were differentiated well between each other in xy- and xz-planes of LMOSEM-SV-PSF. However, the resolution of the point source at distance of 8 cm did not recover although the LMOSEM with SV-PSF were applied.

## 4. Conclusions

Although there was no much difference between the fitness of Gaussian and general parametric models, the general parametric model showed more flexibility dependent on the distance from the Compton camera than Gaussian model. The LMOSEM-SV-PSF gave more improvement on the image quality over the FOV than SIV-PSF for MC data of the combined two and six point sources.

## References

[1]   C. E. Ordonez, C. Wei, and A. Bolozdynya, "Angular uncertainties due to geometry and spatial resolution in Compton cameras," IEEE Trans. Nucl. Sci., 46, pp. 1142-1147, 1999.

[2]   T. Ling, T. H. Burnett, T. K. Lewellen, et al., "Parametric positioning of a continuous crystal PET detector with depth of interaction decoding", Phys. Med. Biol., 53, pp.1843-1863, 2008.

[3]   A. J. Reader, P. J. Julyan, H. Williams, et al., "EM Algorithm System Modeling by Image-Space Techniques for PET Reconstruction," IEEE Trans. Nucl. Sci., 50, pp. 1392-1397, 2003.
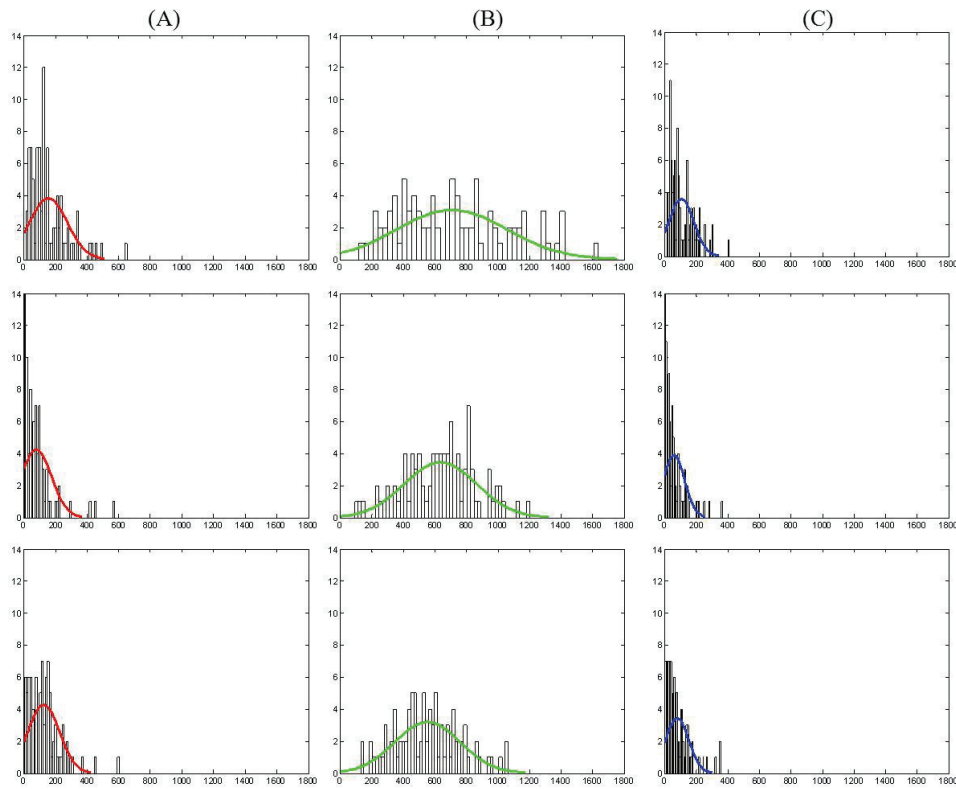
Figure 3. SSR comparison of three PSF functions: (A) Gaussian, (B) Cauchy, and (C) general parametric models (top:x-profile, middle:y-profile, bottom:z-profile).
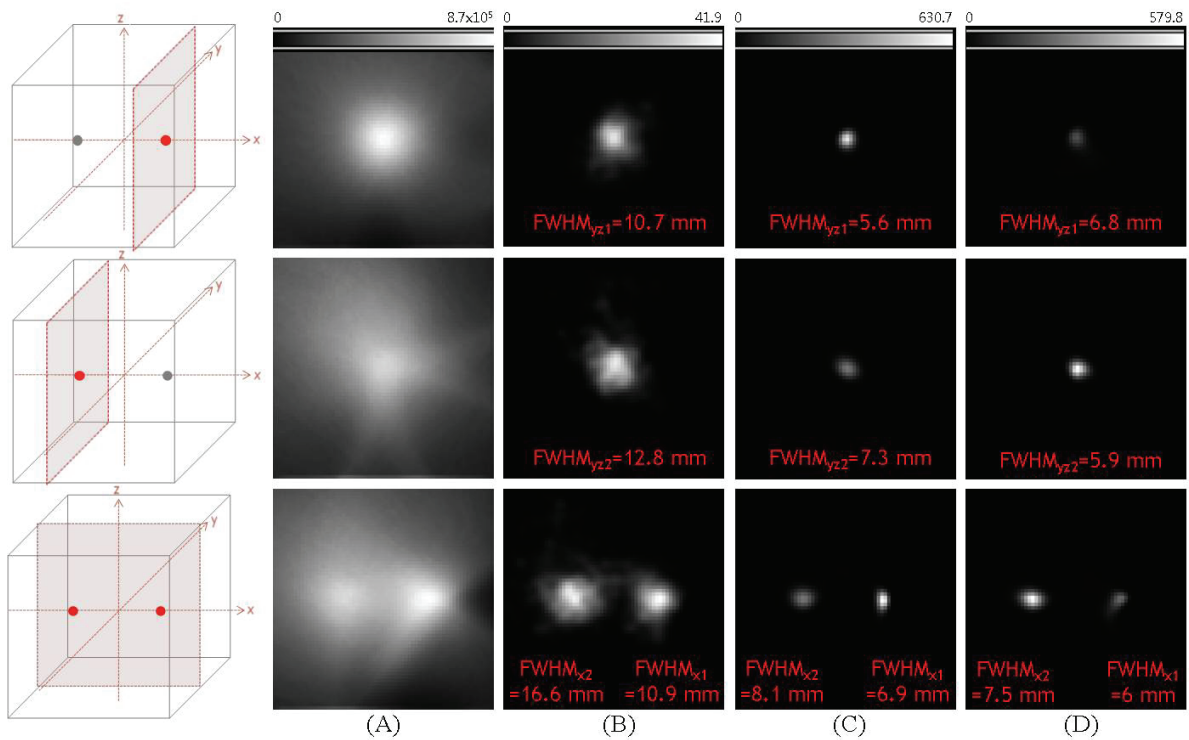


Figure 4. Reconstructed images of two point sources; (A) simple backprojection, LMOSEM (B) without PSF model, with (C) SIV-PSF and (D) SV-PSF.